PHLOWER - Single cell trajectory analysis using Decomposition of the Hodge Laplacian

Mingbo Cheng[1,$], Jitske Jansen[2,3,$], Katharina Reimer[2,3], James Shiniti Nagai[1], Zhijian Li[6,7], Paul Kießling[2], Martin Grasshoff[1], Christoph Kuppe[2,3#], Michael T. Schaub[5,#], Rafael Kramann[2,3,4,#,*], and Ivan G. Costa[1,#,*]

[1]Institute for Computational Genomics, Joint Research Center for Computational Biomedicine, RWTH Aachen University Medical School, 52074 Aachen, Germany
[2]Institute of Experimental Medicine and Systems Biology, RWTH Aachen University, 52062 Aachen, Germany
[3]Division of Nephrology and Clinical Immunology, RWTH Aachen University, 52062 Aachen, Germany
[4]Department of Internal Medicine, Nephrology and Transplantation, Erasmus Medical Center, Rotterdam, Netherlands
[5]Department of Computer Science, RWTH Aachen University, 52074 Aachen, Germany
[6]Gene Regulation Observatory, The Broad Institute of Harvard and MIT, Cambridge, MA, USA
[7]Molecular Pathology Unit, Krantz Family Center for Cancer Research, Massachusetts General Hospital, Boston, MA, USA
[$]co-shared first authors
[#]co-shared last authors
[*]rkramann@ukaachen.de,ivan.costa@rwth-aachen.de

ABSTRACT

Multi-modal single-cell sequencing, which captures changes in chromatin and gene expression in the same cells, is a game changer in the study of gene regulation in cellular differentiation processes. Computational trajectory analysis is a key computational task for inferring differentiation trees from this single-cell data, though current methods struggle with complex, multi-branching trees and multi-modal data. To address this, PHLOWER leverages simplicial complexes and Hodge Laplacian decomposition to infer trajectory embeddings. These natural representations of cell differentiation facilitate the estimation of their underlying differentiation trees. We evaluate PHLOWER through benchmarking with multi-branching differentiation trees and using novel kidney organoid multi-modal and spatial single-cell data. These demonstrate the power of PHLOWER in both the inference of complex trees and the identification of transcription factors regulating off-target cells in kidney organoids.

1 Introduction

Cellular differentiation, the process by which a cell changes its chromatin and expression programs to acquire more specialized functions, is not only crucial in the development of multicellular organisms but also key during onset and progression of diseases. Transcription factors, which are proteins binding to regulatory DNA regions (open chromatin regions), are key regulators of gene expression thereby orchestrating cellular differentiation processes. Dissecting these key regulatory events will help to develop protocols for cellular reprogramming or ex vivo differentiation in e.g. organoids and to understand disease-related differentiation processes for potential therapeutic interventions[1]. In this context, a unique resource to understand the interplay between chromatin, regulatory signals (transcription

factor binding), and expression changes during cellular differentiation[2,3], is multi-modal single-cell sequencing[2], which can measure both full expression programs and genome-wide open chromatin. However, the associated experimental protocols dissociate cells, making it impossible to track how an individual cell differentiates over time experimentally.

To overcome this experimental limitation, computational trajectory analysis, which explores non-linear embeddings in the cellular space and algorithms to find trees in these spaces, has therefore become an important tool in the analysis of cell differentiation in single cells[4–7]. However, these approaches have been hitherto applied to the study of differentiation trees with small trees (3-9 branches) and the only comprehensive benchmarking is based on small trees with four to five differentiation branches[8]. Currently, no work has evaluated their scalability to complex and multi-branching trajectories. Moreover, the analysis of single-cell multiomics data provides further challenges, as there is a need to estimate joint embeddings across modalities for modality detection[9,10]. Altogether, there is a lack of computational approaches to infer complex, branching trajectories from multimodal sequencing data.

We propose here PHLOWER (*decom***P**osition of the **H**odge **L**aplacian for inferring traject**O**ries from flo**W**s of c**E**ll diffe**R**entiation). Hodge Laplacian (HL) matrices are generalizations of the well-known graph-Laplacian explored in diffusion maps[11] and trajectory inference for single cell data[12,13]. HL are algebraic representations of simplicial complexes, generalizations of graphs that allow not only for nodes and edges, but also triangles and other higher-order structures to be present. The spectral decomposition of HL matrices, specifically of the L_1 Hodge-Laplian allows the creation of embeddings on the edge (cell differentiation events) or trajectory space (cell differentiation paths)[14]. These represent cell differentiation processes more naturally, and can thus enable the detection of complex differentiation trees and characterize branching events with high precision.

2 Results

2.1 Differentiation Tree Inference with PHLOWER

PHLOWER uses the Hodge Laplacian (HL) and its associated Hodge decomposition to obtain embeddings of cell differentiation trajectories. The Graph Laplacian (a zero-order Hodge Laplacian) is a matrix representation of graphs, where samples are encoded as vertices and distances as edge weights, representing the nonlinear manifold of gene expression space. The dominant eigenvectors of the zero-order Graph Laplacian are used to analyze this manifold, forming the basis for methods in clustering analysis[15], manifold learning[11], trajectory inference and pseudo-time estimation in single-cell data[12,13]. In PHLOWER, we employ a representation of single cell data as a simplicial complex, i.e., a higher-order generalization of a graph, consisting of nodes (0-simplices), edges (1-simplices) and triangles (2-simplices). The spectral decomposition of the HL can be used to decompose flows and trajectories[14,16] on the edges into gradient, curl, and harmonic components of the gene expression manifold. Of particular interest in our context here are the spectral embeddings induced by the so-called harmonic eigenvectors of the HL[14,16] as these are associated to holes in the simplicial complex, which in turn can reveal cell differentiation tree branches in the gene expression embedding (see methods for more details).

In short, PHLOWER first uses a graph representation of the single cell data and (zero order) Laplacian to estimate pseudo time of cells and identify progenitor and terminal cells. Cell differentiation processes are classically thought of as generating an out-branching, tree-like structure. To transform such a directed branching process into a simplicial complex, we perform a Delauney triangulation and connect terminal differentiated cells (high pseudotime) with progenitor cells (low pseudotime), which creates holes for every main trajectory in the graph (Fig. 1). Next, we

perform a Hodge Decomposition of this simplex, which provides edge level embeddings, where each point in an embedding represents a cell differentiation event, as well as a trajectory embedding, where each embedding point represents a cell differentiation trajectory. PHLOWER explores these embeddings to delineate major differentiation trajectories in single-cell data and to reconstruct complex cell differentiation trees. As an example, we show how PHLOWER can be used to predict a simple differentiation tree from mouse embryonic cells (MEF) towards either neurons or myocytes (Fig. 1 and Supp. Fig. S1).

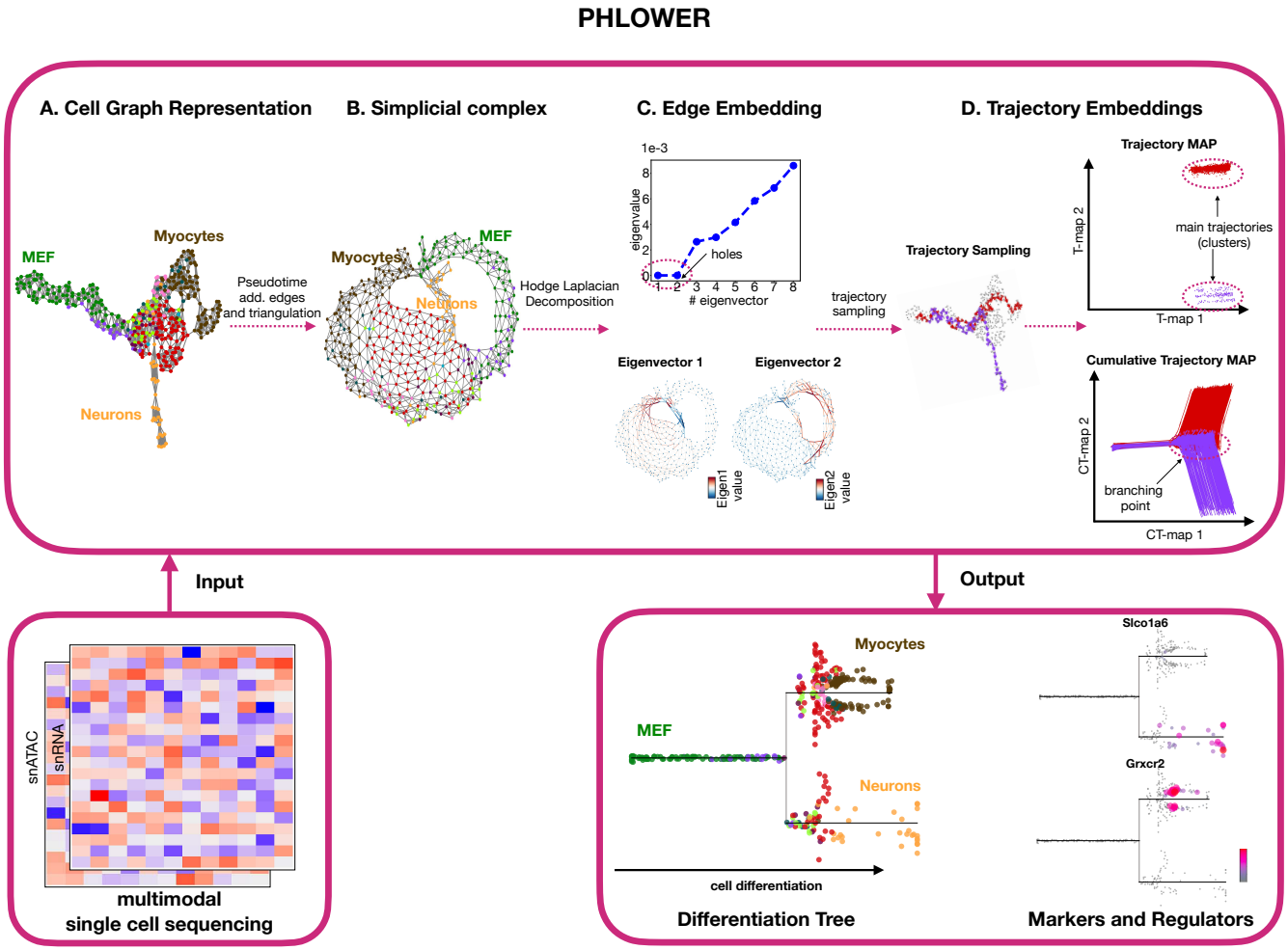

Figure 1. Schematic overview of major steps of PHLOWER . PHLOWER receives as input a multimodal or an unimodal single cell dataset. **(A)** It next creates a graph representation and a graph embedding[17] of the cells. Our example is based on a differentiation system of mouse embryonic fibroblasts (MEF) towards neurons or myocytes[18]. From this graph, PHLOWER uses a zero order Laplacian decomposition and random-walk to estimate pseudo-time from progenitor cells (i.e. MEF). **(B)**, Next, cells with low (progenitors) and high pseudotime (terminally differentiated cells) are connected and a simplicial complex (SC) is obtained by Delaunay triangulation of the graph. **(C)** An edge embedding is obtained via the decomposition of the Hodge-Laplacian. In the MEF data, the first two eigenvectors have zero eigenvectors and their signals discriminate edges belonging to the two differentiation trajectories (or holes in the SC). **(D)** PHLOWER performs next random walks to obtain trajectories and uses the HL decomposition to obtain a trajectory embedding and a cumulative trajectory embedding. Clustering analysis in the trajectory embedding reveals major trajectories in the data, while the cumulative embedding space is used to estimate trajectory backbones and branching point events. PHLOWER outputs stream trees representing the differentiation tree over pseudo-time and allow the detection of regulators and gene markers.

Benchmarking of Trajectory Inference Methods

Next, we evaluated PHLOWER and competing methods on simulated datasets[19] on how well methods can recover original tree structures and how well they can place cells within these differentiation trees. We utilized the diffusion-limited aggregation tree (DLA tree)[19] to simulate ten complex differentiation tree dataset with 5 to 18 total branches similar as in[13]. These data were provided as input for PHLOWER and competing approaches for the detection of differentiation trees (PAGA tree[4], monocle 3[20], cellTree[21], pCreode[22], Slice[23], RaceID/StemID[24,25], slingshot[6], TSCAN[26], Slicer[27], MST[28], Elpigraph[29], and STREAM[5]). This selection included the top 10 approaches from a recent benchmark evaluation[30]. [1] Tools were evaluated using the metrics proposed by the Dynverse framework[30]: tree structure similarity (Hamming-Ipsen-Mikhailov; HIM), location of cells within a branch (Correlation), cell allocation to branches (F1 branches), and cell allocation to branching points (F1 milestones).

PHLOWER was the best-performing method in regard to tree topology recovery, followed by PAGA, RaceID/StemID and monocle (Fig.2A). In the problem of allocating cells to positions in a branch, PHLOWER was also the best performer, followed by TSCAN and RaceID (Fig.2B). In the problem of allocating cells to the correct branches, PHLOWER obtained the best performance, followed by monocle and PAGA. Finally, in the allocation of cells to branches, PHLOWER was the best performer, followed by RaceID/StemID, monocle, and PAGA. Altogether, PHLOWER was ranked as the top performer in all evaluated scenarios. An example of the steps of the PHLOWER algorithm in fitting a differentiation tree in a simulated data is shown in Supp. Fig. S2. A runner-up method was RaceID/StemID[24,25] which also ranked within the top four methods in all scenarios. The performance of PHLOWER and competing methods is illustrated by the visualisation of the tree backbones on simulated data with six final branches as provided by dynverse (Fig. 2E-F; Supp. Fig. S3).

Inferring cellular trajectories in kidney organoids

Induced pluripotent stem cell (iPSC) derived kidney organoids represent a solid model to validate cellular trajectories since this model represents the differentiation of stem and progenitor cells towards various kidney cell lineages. We therefore generated a multimodal single cell multiome sequencing (RNA and ATAC) data sets of kidney organoids after 7, 12, 19 and 25 days of differentiation by using an own protocol[32]. This recovered 13,751 cells with an average of 10,378 RNA transcripts and 19,263 DNA fragments (ATAC) per cell (Supp. Fig. S4). We next integrated the data for each modality independently[33] and used MOJITOO to obtain a joint ATAC-RNA embedding[9]. We provided the data as input for PHLOWER, which recovered a trajectory with nine branches (Fig. 3A; Supp. Fig. S5). We observed that the tree successfully sorted cells based on the organoids age (Fig. 3B) and this matched well with the pseudo-time estimates (Fig. 3C). These nine branches could be grouped into three major branches associated with epithelial cells (two sub-branches associated with podocytes and one with tubular cells); four branches of stromal cells and one major branch associated with muscle and neuronal cells (3 sub-branches). The annotation of these cells was based on the expression of markers as TBXT[34] and KDR[35] for mesoderm cells; PODXL[36] and NPHS2[36] for podocytes, SLC12A1[37] and PAPPA2[37] for kidney tubule epithelial; COL1A2[36] and PDGFRA[38] for stromal cells; and neuronal and muscle markers MAP2[32], MSX1[34,36–38], MYL1 and MYF6 (Supp. Fig. S6). The latter branches, i.e. neuronal and muscle, are considered off-target cells and potentially may hamper maturation of kidney cells in the organoids, which should be avoided in kidney orgnoids[39,40].

A key question to be addressed by PHLOWER is the detection of regulators (transcription factors; TF) driving the differentiation of iPSC within the kidney organoids. We leveraged here both the trees inferred by PHLOWER

[1] Note that some tools (Palantir and MIRA[7,31]) do not infer differentiation trees and can therefore not be evaluated here.

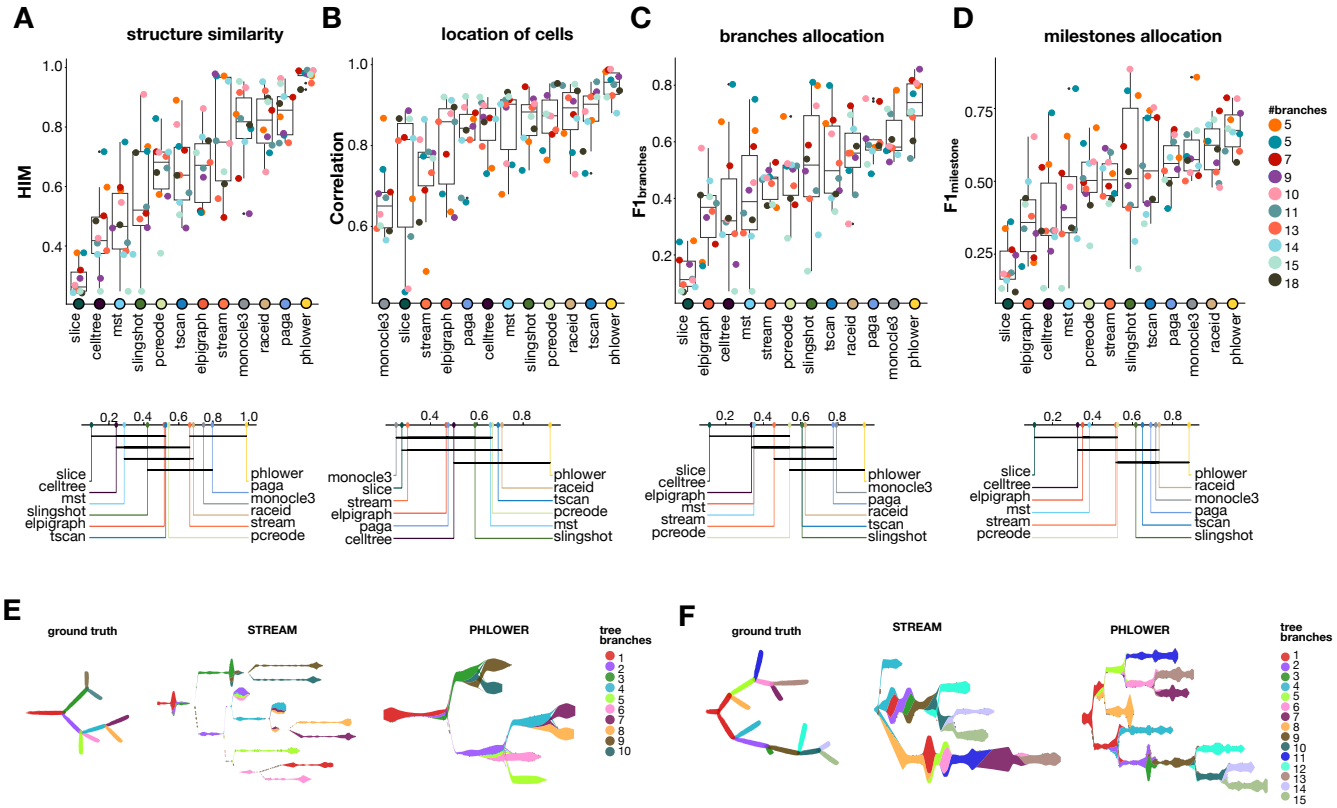

Figure 2. PHLOWER benchmarking. A) We show the HIM score (y-axis) for all 12 tree inference algorithms (x-axis) (top) measuring topology similarity between true and inferred trees. Methods are ranked (left to right) regarding the median value. We show below the mean ranking of the methods, while bars indicate methods with similar performance. Higher ranking values indicate the best performer. **B-D)** Same as **A** cell allocation within a branch (correlation); Cell allocation to branching points (F1 milestones) and cell allocation to branches (F1 branches). **E)** Differentiation trees estimated with STREAM and PHLOWER algorithms for the 10 branches data. **F)** Similar to E from 15 branches of DLA tree data.

to find TFs related to branch differentiation using a procedure similar to scMega[41]. In short, we estimated TF activity scores with ChromVAR[42] and selected TFs, which expression are concordant with the TF activity and are differential expressed between compared branches (Supp. Fig. S7). When comparing cells at the end of tubular and podocyte trajectories, this recovered bonafide regulators of these cells such as WT1[43] and MAFB[44] for podocytes and HNF1B[45] and GRHL2[46] for tubular cells (Fig. 3E and Supp. Fig. S8). Next, we compared major branches: stromal cells vs. others and neuronal/muscle cells vs. others. We detected TFs related to fibroblasts TWIST1 and RUNX2[47,48] as regulators of stromal cells, and the known skeletal muscle MYOG for the muscle branch. Among the top three neuronal cells regulators, we observed the TFs PAX3, RFX4 and ZIC2, which have been previously related to neuronal cell differentiation and/or neuronal diseases[49–51]. The modulation of these TFs is of particular interest, as neuronal cells are considered to be undesired off-target cell types in kidney organoids.

Spatial organization of kidney organoids and perturbation of off-target lineages

We leveraged our analysis of multimodal single cell data to perform a subcellular resolution spatial transcriptomic analysis of kidney organoids using the Xenium spatial imaging platform[52]. We used PHLOWER results to derive a 100 gene kidney organoid marker panel for the detection of mesenchymal, tubule-epithelial, stromal, neuronal cells

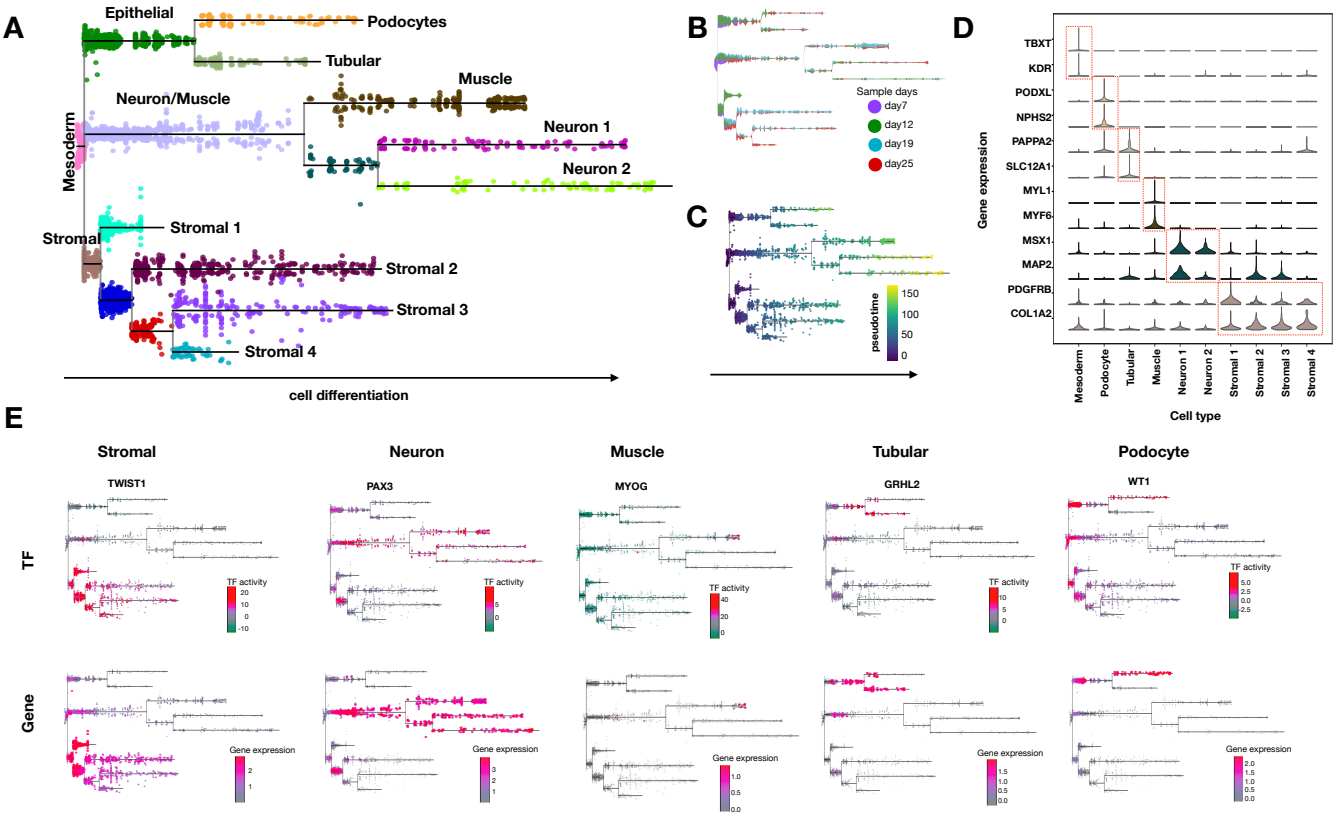

Figure 3. Kidney organoid data. A) Differentiation tree on the kidney organoid data as estimated by PHLOWER. **B-C)** Day of differentiation and pseudo-time estimates of cells in the differentiation trees. **D)** Violin plots show the marker genes for cell types in each branch. **E)** We show selected TFs with branch specific expression and TF activity scores.

and podocytes (Sup. Fig. S9A). This panel selection included computational data driven based marker genes from the multiome analysis and some literature based marker genes; and top candidate TFs from the scMega analysis (Supp. Table S1).

Clustering and trajectory analyses of the 105,092 cells in a 19 day kidney organoid and two 25 days kidney organoids indicated the identification of progenitor cells (mesoderm progenitors podocyte and tubule-epithelial progenitors) and all major kidney organoid branches (mesoderm, podocytes, tubule-epithelial-cells, stromal and neuronal-cells) (Fig. 4A-B; Supp. Fig. S9C). When contrasting cells detected on 19 vs. 25 days, we observed a higher proportion of mesoderm cells in day 19; while day 25 had a higher amount of tubule-epithelial cells and podocytes (Fig. 4C)reflecting the higher maturation of organoids at day 25. Moreover, we observed gene and TF expression patterns similar to the predictions based on the multi-modal analysis (Fig.4D and Supp. Fig. S9D-E;S12;S11). This included the TFs PAX3, RFX4 and ZIC2, which were predicted by PHLOWER to control the off-target neuronal lineage. Altogether, these results indicate that the Xenium panel can identify major differentiation branches in kidney organoids in a spatial context and will aid in understanding cell differentiation differences based on signaling events originating from cellular neighborhoods and spatial niches.

To validate PHLOWER predictions, we performed multiplex siRNA knockdown experiments of the identified neuronal lineage defining TFs PAX3, RFX4 and ZIC2 in kidney organoids in iPSC derived kidney organoids during the differentiation process from day 12 onwards. Knock-down experiments led to a reduction of 25-30% in PAX3,

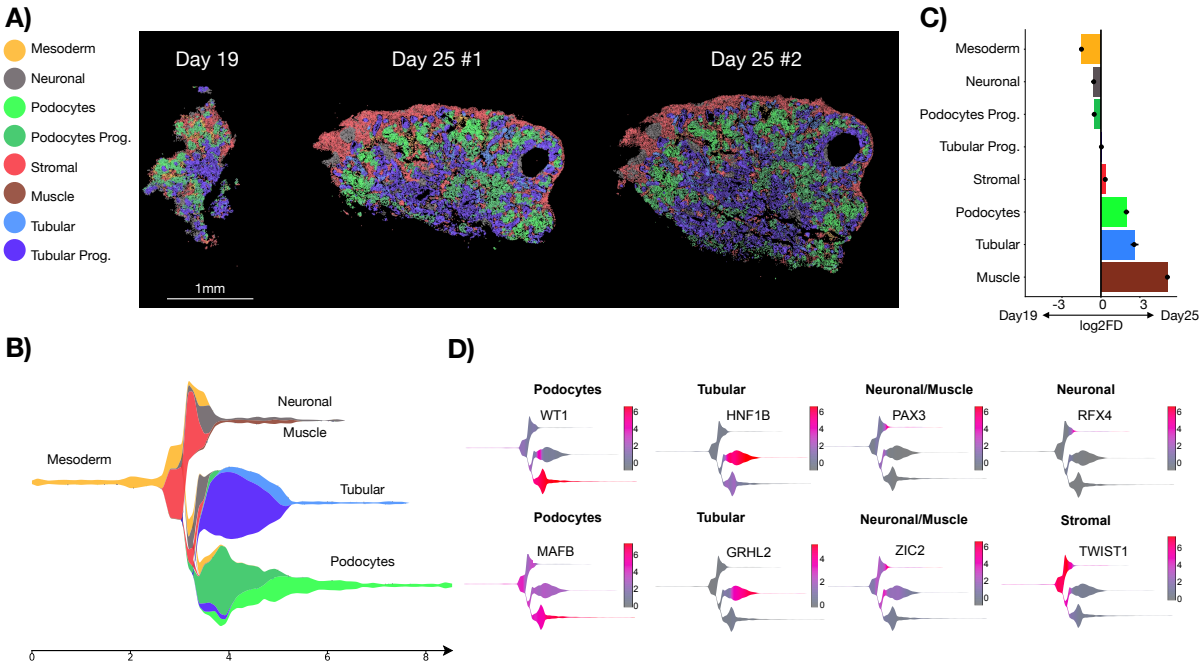

Figure 4. Spatial Profiling of Kidney Organoids A) We show Xenium based spatial profiling of kidney organoids differentiation at day 19 and day 25 (section #1 and #2). Colors represent distinct cell populations. **B)** PHLOWER estimated differentiation tree on day 19 & day 25 organoids. **C)** Single cell proportion test comparing cell abundances in day 25 vs day 19. Error bars are based on confidence intervals for the magnitude difference returned via bootstrapping[53]. **D)** TFs controlling the differentiation of the kidney organoid branches.

RFX4 and ZIC2 mRNA expression (Supp. Fig. S10). Xenium spatial profiling of scrambled siRNA as control condition (scrambled; 2x section) and siRNA treated organoids against PAX3, RFX4 and ZIC2 detected the same cell types as non-treated day 25 organoids (Fig. 5A). When contrasting scrambled siRNA vs siRNA, we observed a significant increase of tubular cells and podocyte progenitors and a significant decrease of muscle, stromal and neuronal cells (Fig. 5B). Immunofluorescence staining further confirmed the reduction of stromal cells including off target neuronal cells in siRNA condition, as reflected by the significant decrease in interstitial vimentin (Fig. 5C-D). We observed a significant increase in podocyte nephrin protein expression and 50% more tubular E-cadherin protein expression, suggesting improved podocyte (progenitor) and tubular characteristics as a result of diminished off-target cells (Fig. 5E). Altogether, these experiments supported the that gene silencing of PAX3, RFX4 and ZIC2 known as neuronal lineage markers and considered as an off-target population, led to a small increase in tubular cell proportion and enhanced podocyte development as shown by increased nephrin and a higher cell proportion of podocyte progenitors.

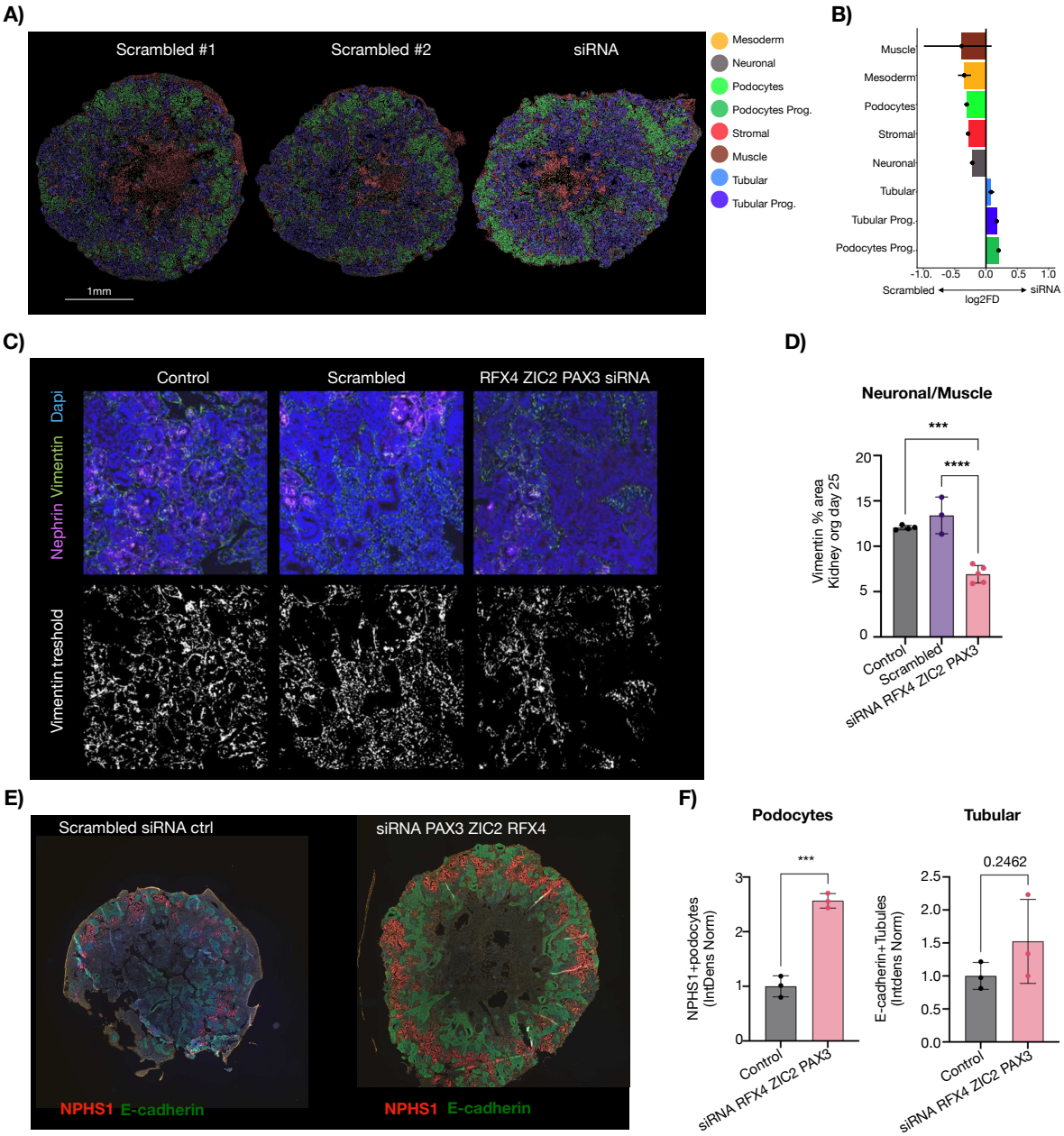

Figure 5. Spatial profiling of kidney organoids after siRNA knockdown of PAX3, RFX4 and ZIC2. A) We show Xenium based spatial profiling of kidney organoids at Day 25 after treatment with scrambled siRNA control (scrambled) and siRNA multiplex against the TFs PAX3, RFX4 and ZIC2 (siRNA). **B)** Single cell proportion test comparing cell abundances in siRNA and scrambled siRNA kidney organoids. Error bars are based on confidence intervals for the magnitude difference returned via bootstrapping[53]. **C)** Immunoflurecence staining of control. scrambled siRNA and siRNA treated kidney organoids showing nephrin (magenta), vimentin (green), and dapi (blue). **D)** Quantification of the neuronal marker vimentin^{+}, NPHS1^{-} of images of (C) using one-way ANOVA analysis followed by Tukey post-test with bars representing mean ± sd; asterisks indicate P-values of <0.001(***), <0.0001(****). **E)** Silencing of RFX4, ZIX3 and PAX3 increased nephrin (red) expression in podocytes and increased e-cadherin (green) expression in tubular cells by 50%, though not significant. **F)** Podocyte and tubule quantification using unpaired *t*-test with bars representing mean ± sd; asterisks indicate P-values of <0.001(***).

3 Discussion

Trajectory analysis is paramount in the analysis of cells undergoing cell differentiation. Despite a wealthy literature of computational methods[8], most methods have been only applied or tested in small cell differentiation trees with few branches. PHLOWER explores the unique Hodge Laplacian decomposition, which allows to consider the interaction between edges of a simplicial complex in order to estimate embedding on edges and trajectories levels. By exploring this higher order representation of the data in a more natural way, it allows the detection of complex and large cell differentiation trees, as supported by our benchmarking analysis.

Multimodal single cell data, which allows the parallel measurement of transcriptome and open chromatin data, can provide rich information on the relationship between regulatory and transcription function of cells[3]. We display the power of PHLOWER by analysing a kidney organoid differentiation course, where PHLOWER was able to detect major cell lineages, as well as TFs with branch specific gene expression and TF activity. We leveraged gene markers from PHLOWER predicted lineages to delineate a gene panel for uncovering the architecture of kidney organoids using in-situ sequencing spatial profiling. A particular important aspect of organoid growth is to improve protocols via the modulation of particular lineages[39,40,54]. Undesired off-target populations have been described to hamper kidney organoid development[39,40,54]. Targeting these populations using genetic or pharmacological perturbations led to improved organoid development and maturation. Here, we used siRNA targeting TFs controlling neuronal cells, as identified by PHLOWER, to reduce the abundance of these off-target cell types in kidney organoids and improved tubular cell formation. This reinforces the ability of reinforces the ability of PHLOWER to uncover regulators in complex cell differentiation systems. An interesting future venue of research is to adapt PHLOWER to explore cellular barcoding[55].

4 Methods

4.1 Rationale

PHLOWER uses the Hodge Laplacian (HL) and its associated Hodge decomposition to obtain embeddings of cell differentiation trajectories. Graph Laplacians (zero-order Hodge Laplacians) are matrix representations of graphs, and form the basis for a wealth of methods for clustering analysis and manifold learning[11,15], which are commonly used for trajectory inference and pseudo-time estimation in single cell data[12,13]. Specifically, by encoding samples (cells) as vertices and distances between samples (cells) as edge weights, we can construct a graph that can serve as a proxy for the nonlinear manifold underlying the gene expression space. The dominant eigenvectors of the associated graph Laplacian can then be used to analyse this gene expression manifold in more detail, in terms of clusters and latent dimensions.

In PHLOWER, we employ a representation of single cell data as a simplicial complex, i.e., a higher-order generalization of a graph, consisting of nodes (0-simplices), edges (1-simplices) and triangles (2-simplices). We can then use the (first) Hodge Laplacian (HL), a higher-order generalization of the graph Laplacian, to understand flows and trajectories[14,16] on the gene expression manifold. This enables us to build low dimensional representations of cell differentiation data, representing cell differentiation events and differentiation trajectories (or paths) on the gene expression manifold. See Supp. Fig. S15 for a graphical contrast of the L0 and L1 Laplacian decompositions.

Rather than assessing how nodes are connected to each other via edges, the first-order HL describes how edges relate to each other via nodes (so-called lower-adjacency) and triangular faces (upper-adjacency). Importantly, the spectral decomposition of the HL can be used to decompose flows and trajectories on the edges into gradient, curl,

and harmonic components, akin to the classical Helmholtz decomposition of vectors fields known from vector calculus. Just like the eigenvectors of the graph Laplacian can be used to define a spectral embedding of the nodes in a graph, the eigenvectors of the Hodge-Laplacian can be used to provide a spectral embedding of the edges. As edges correspond to cell differentiation events this enables us to study cell differentiation events and cell differentiation pathways (sequences of edges) in a natural way. Of particular interest in our context here are the spectral embeddings induced by the so-called harmonic eigenvectors of the HL[14,16], as these are associated to "holes" in the underlying space.

4.2 PHLOWER

PHLOWER receives as input a set of matrices representing a single cell sequencing modality that is:

$$\mathcal{X} = \{X^{(1)}, \cdots, X^{(m)}\} \tag{1}$$

where $X^{(i)} \in \mathbb{R}^{n \times s^{(i)}}$ represents the data of a particular single cell modality, n represents the number of cells, and $s^{(i)}$ represents the number of features in modality i. Here, we assume that cells match across modalities. PHLOWER has been evaluated on multimodal single cell (ATAC and RNA) sequencing or unimodal scRNA-seq ($m = 1$). First, PHLOWER constructs a graph representation G of the single cell matrix by estimation of a joint embedding[9] followed by kernel representation, graph construction and pseudo-time estimation as before[56]. Next, it builds a simplicial complex (SC). For this, we first use the Delaunay triangulation procedure between nodes (cells), we next use pseudo-time information from the graph to find terminal differentiated cells from root cells. Finally, we connect terminal (differentiated) cells to root (progenitors) cells with edges to create holes to obtain the final SC.

We next count edges and triangles of this SC and perform a spectral analysis of the harmonic decomposition using normalized Hodge 1-Laplacian[14]. Dominant eigenvectors delineate holes in the SC, which are associated with cell differentiation trajectories in the SC. Lastly, we sample trajectories from the SC to obtain paths (or edge flows). Dot product of paths with the harmonic spaces creates a trajectory embedding, where each point represents a particular trajectory. Clustering analysis on this space allows PHLOWER to find major trajectories. Moreover, it builds a cumulative trajectory space, which is used to recover the differentiation trees, which can be visualised as stream plots[5]. PHLOWER outputs a tree structure, the association of each cell within a branch and pseudo-time estimates (Supp. Fig. S1). It also detects branch specific regulators by detection of TFs similar as in[41] with: (1) branch specific expression patterns and (2) similar gene expression and TF activity[42] along the cell differentiation.

4.3 Single Cell Graph Representation

As a first step, PHLOWER estimates a single cell graph to represent the data using a procedure similar to DDHodge[56]. This procedure receives a low-dimensional embedding X^l, which can be provided by MOJITOO[9] for multi-modal data; or by principal component analysis (PCA) for scRNA-seq.

4.3.1 Diffusion Map

Given a common cell joint embedding X^l, we represent the data as a diffusion map[11]. For this, we first estimate a Gaussian kernel W:

$$W_{ij} = \exp\left(-\frac{\|x_i^l - x_j^l\|^2}{\sigma_i \sigma_j}\right) \tag{2}$$

where x_i^l is the representation of sample (cell) i in the embedding X^l and σ_i is the local scaling parameter. This is estimated with the distance to the n-th nearest neighbor from x_i^l as in[57].

The (zero-order) Graph Laplacian L_0 can be defined as:

$$L_0 = D - W \tag{3}$$

where D is a diagonal matrix that the i-th entry $d_{ii} = \sum_j W_{ij}$. The random walk on graph laplacian L_0 we can reach the steady state[58] where

$$p_{t+1} = p_t D^{-1} W \equiv p_t M \tag{4}$$

where $p_t \in \mathbb{R}^n$ is normalized probability vector, M is transition matrix of the graph. Next, we perform an eigendecomposition on the symmetric form of M such that:

$$M' = D^{\frac{1}{2}}(M)D^{-\frac{1}{2}} = D^{\frac{1}{2}}(D^{-1}W)D^{-\frac{1}{2}} = D^{-\frac{1}{2}}WD^{-\frac{1}{2}} = Q\Lambda Q^\top \tag{5}$$

Taking advantage of the above eigendecomposition, we can effectively calculate M^s (see[11]), such that:

$$M^s = (D^{-\frac{1}{2}}M'D^{\frac{1}{2}})^s = (D^{-\frac{1}{2}}Q\Lambda Q^\top D^{\frac{1}{2}})^s = D^{-\frac{1}{2}}Q\Lambda^s Q^\top D^{\frac{1}{2}} \tag{6}$$

where the columns of $D^{-\frac{1}{2}}Q$ include the right eigenvectors of M and the rows of $Q^\top D^{\frac{1}{2}}$ include the left eigen vectors. The diagonal matrix Λ contains the corresponding eigenvalues.

Finally, we can estimate pseudotime u (or potential) at time $t = s$ as:

$$u = (1/m, 1/m, \cdots, 1/m, 0, 0, \cdots, 0)M^s \tag{7}$$

where m is the number of start cells, and s is the diffusion process at the time $t = s$.

4.4 Graph based pseudotime estimation

To improve the pseudotime estimates, we use a procedure similar to[56], which smooths pseudo-time estimates by considering the graph connectivity. For this, we define initial edge weights as gradient values of the fully connected graph, e.g. $w_{ij}^F = u_j - u_i$. Next, we prune this fully-connected graph by considering only the k nearest neighbors. This provides a graph $G^{(knn)} = (\mathcal{V}, \mathcal{E})$, where $\mathcal{V}$ is the set of vertices and $\mathcal{E}$ is the set of edges. We represent this graph as an incidence matrix $\mathbf{B_1}$. For vertex $v_j \in \mathcal{V}$ and edge $e_i \in \mathcal{E}$, we have:

$$B_1[i,j] = \begin{cases} -1 & \text{if edge } e_j \text{ leaves vertex } v_i \\ 1 & \text{if edge } e_j \text{ enters vertex } v_i \\ 0 & \text{if otherwise.} \end{cases} \tag{8}$$

This is used to define the incidence matrix for full graph and pruned k-nn graph respectively $\mathbf{B_1}^F$ and $\mathbf{B_1}^P$. We want to estimate pseudo-times of the pruned k-nn graph by using the pseudo-time estimates of the full graph. For this, we

get a first estimate of the gradients of the truncated graph (w^P) by minimizing:

$$\min_{w} \frac{1}{2}\|\mathbf{B_1}^F w^F - \mathbf{B_1}^P w^P\|^2 + \frac{\lambda}{2}\|w^P\|^2, \tag{9}$$

where λ is the regularization parameter. Next, we update the potential of the vertices

$$u' = \arg\min_{u'} \|(\mathbf{B_1}^P)^\top u' - w^P\|^2. \tag{10}$$

This allows us to estimate an updated gradients $w^s = \mathbf{B_1}^\top u'$. Next, we use these gradients to estimate the final pseudotime u^s of the vertices as:

$$u^s = \arg\min_{u^s} \|\mathbf{B_1}^\top u^s - w^s\|^2. \tag{11}$$

With the graph $G^{(knn)}$ with edge weights w^s and pseudotime estimates u^s, we estimate a diffusion embedding with the stress majorization layout algorithm[17,59]. Examples of the graph layouts and pseudo-time estimates can be seen in Supp. Fig. S1A.

4.5 Hodge Laplacian Decomposition on a Single Cell Simplicial Complex

Given $G^{(knn)}$ and pseudo-time estimate u^s, the next steps are the creation of a simplicial complex and estimation of the Hodge Laplacian decomposition.

4.5.1 Triangulated Single cell graph

A typical cell differentiation graph has tree-like structures. Laplacian decomposition are able to find distinct types of topological structures (connected components, holes, voids), but not trees or branches. PHLOWER resorts to a simple trick, i.e. it uses pseudo-time estimates to find end-state cells and adds dummy/artificial edges from end-state to start state cells. This creates holes in the data, one for each trajectory in the tree. For this, we obtain m (default 5) cells with highest and lowest pseudotime. We include directed edges from terminal (high pseudotime) to start (low pseudo-time) vertices. Next, we use a Delaunay triangulation[60] on the diffusion embedding to create uniformly distributed set of triangles around the single cell graph by first ignoring the dummy edges. Next, we remove edges connecting distant cells, i.e. we estimate the distribution of distance of connected vertices and obtain the value associated with the 75% quantile (Q_{75}) and we remove all edges connecting vertices, which distance is higher than $3 \times Q_{75}$. We further refine the dummy edges by performing a triangulation between each pair of terminal cells and root cells. This results in a triangulated graph $G^{(t)} = (\mathcal{V}^{(t)}, \mathcal{E}^{(t)}, \mathcal{T}^{(t)})$, where $\mathcal{V}^{(t)}$ is the vertices set, $\mathcal{E}^{(t)}$ is the edge set of graph $G^{(t)}$ and $\mathcal{T}^{(t)}$ is the set of triangles. A triangle can be loosely defined as a 3-vertex clique, i.e. three nodes fully connected by edges. An example of the simplex representation of a differentiation tree is provided in Supp. Fig. S1B.

4.5.2 Simplicial Complex

For a given triangulated graph $G^{(t)}$, the next task is to obtain a second order simplicial complex (SC). A simplicial complex is a set composed of vertices (0-simplices), edges (1-simplices) and triangles (2-simplices) and their k-dimensional counterparts. These can be represented by the estimation of incidence matrices, or boundary operations $\mathbf{B}_k$ which maps $k-1$ simplices to k simplices. For example, $\mathbf{B}_1$ captures the relation between vertices (0-simplices) and edges (1-simplices) and $\mathbf{B}_2$ captures the relation between edges (1-simplices) and triangles (2-simplices)[61].

The boundary matrix on 1-simplices $\mathbf{B}_1$ is defined as in Eq. 8. An entry in $\mathbf{B}_2$ capturing the relationship between an directed edge $e_i \in \mathcal{E}$ and a directed triangle $\triangle_q \in \mathcal{T}$ can be defined as:

$$B_2[i,q] = \begin{cases} -1 & \text{if } e_i \in \triangle_q \text{ and } e_i \text{ has same direction as the triangle} \triangle_q \\ 1 & \text{if } e_i \in \triangle_q \text{ and } e_i \text{ has opposite direction than the} \triangle_q \\ 0 & \text{if otherwise.} \end{cases} \tag{12}$$

Check figure S16 for an example of a simplicial complex and its corresponding $\mathbf{B}_1$ and $\mathbf{B}_2$ matrices. There we can find several edges ([1,2], [2,3], [2,4], [2,5], [3,4], [4,5], [4,6], [4,7], [6,7], [7,8]) and 3 triangles ([2,3,4], [2,4,5] and [4,6,7]). Entry $B_1[1,1]$ has value -1, as the first edge $e_1 = (1,2)$ leaves vertex 1, while $B_1[2,1]$ has value 1, as the first edge $[1,2]$ enters the vertex 2. Regarding $\mathbf{B}_2$, all entries related to the first edge $e_1 = (1,2)$ are zero, as there is no triangle associated to it. $B_2[2,1]$ is equal to one as the direction of $e_2 = (2,3)$ fits the direction of the first triangle ($\triangle_1 = (2,3,4)$). $B_2[3,1]$ is equal to -1 as the third edge ($e_3 = (2,4)$) has opposite direction to $\triangle_1 = (2,3,4)$. We refer the reader to[14] for a in depth characterization of simplicial complexes.

Here, we are only interested in the direction of edges (flows) and the direction of triangles are only used for bookkeeping, i.e. their directions follow the index of the vertices in increasing order. Note also that the boundary operation requires less memory than adjacency matrices for sparse graphs, i.e. $\mathbf{B}_1$ is smaller than a graph incidence matrix if the number of edges is smaller than the number of vertices. A similar rationale follows for $\mathbf{B}_2$.

4.5.3 Hodge Laplacian and decomposition

Hodge Laplacian is a higher order generalized form of graph Laplacian, for a graph G, The k-th hodge Laplacian is:

$$L_k = \mathbf{B}_k^\top \mathbf{B}_k + \mathbf{B}_{k+1}\mathbf{B}_{k+1}^\top \tag{13}$$

where $\mathbf{B}_k$ is the incidence matrix.

For $k = 0$, L_0 is the same as the zero order graph Laplacian introduced in Eq. 14.

$$L_0 = \mathbf{0}^\top \mathbf{0} + \mathbf{B}_1\mathbf{B}_1^\top = \mathbf{D}_1 - \mathbf{A}, \tag{14}$$

where $\mathbf{D}_1$ is the diagonal matrix of a graph and $\mathbf{A}$ is the adjacency matrix.

Here, we are interested in the first order Hodge Laplacian, i.e.:

$$L_1 = \mathbf{B}_1^\top \mathbf{B}_1 + \mathbf{B}_2\mathbf{B}_2^\top. \tag{15}$$

As in diffusion maps[19], it is preferable to work with the normalized form of the Hodge Laplacian, as this provides a random walk process on the simplex[14]:

$$\mathcal{L}_1 = \mathbf{D}_2\mathbf{B}_1^\top \mathbf{D}_1^{-1}\mathbf{B}_1 + \mathbf{B}_2\mathbf{D}_3\mathbf{B}_2^\top \mathbf{D}_2^{-1} \tag{16}$$

where $\mathbf{D}_2$ is the diagonal matrix of (adjusted) degrees of each edge, i.e. $\mathbf{D}_2 = \max\left(\text{diag}(|\mathbf{B}_2|\mathbf{1}), \mathbf{I}\right)$. $\mathbf{D}_1$ is the diagonal matrix of weighted degrees of the vertices, and $\mathbf{D}_3 = \frac{1}{3}\mathbf{I}$. Like the standard form of $\mathcal{L}_0$, here $\mathcal{L}_1$ is asymmetric which

makes eigen-decomposition hard. To address this, we construct the symmetric form of $\mathcal{L}_1$ as following:

$$\mathcal{L}_1^s = \mathbf{D}_2^{-1/2}\mathcal{L}_1\mathbf{D}_2^{1/2} = \mathbf{D}_2^{1/2}\mathbf{B}_1^\top\mathbf{D}_1^{-1}\mathbf{B}_1\mathbf{D}_2^{1/2} + \mathbf{D}^{-1/2}\mathbf{B}_2\mathbf{D}_3\mathbf{B}_2^\top\mathbf{D}_2^{-1/2}. \tag{17}$$

Next, we perform eigendecomposition on the symmetric form $\mathcal{L}_1^s$ such that:

$$\mathcal{L}_1^s = Q\Lambda Q^\top \tag{18}$$

where columns of Q are the eigenvectors and the diagonal elements of the diagonal matrix Λ indicate the corresponding eigenvalues. Thus the decomposition of the normalized form $\mathcal{L}_1$ becomes:

$$\mathcal{L}_1 = \mathbf{D}_2^{1/2}\mathcal{L}_1^s\mathbf{D}_2^{-1/2} = \mathbf{D}_2^{1/2}Q\Lambda Q^\top\mathbf{D}_2^{-1/2} = \mathbf{U}\Lambda\mathbf{U}^{-1} \tag{19}$$

where $Q \in \mathbb{R}^{\|\mathcal{E}^{(t)}\|\times\|\mathcal{E}^{(t)}\|}$ is the eigenvector of $\mathcal{L}_1^s$, $\|\mathcal{E}^{(t)}\|$ is the number of edges in graph $G^{(t)}$, the diagonal matrix $\Lambda \in \mathbb{R}^{\|\mathcal{E}^{(t)}\|}$ records the corresponding eigenvalues. We can make use of the right eigenvector $q_R = \mathbf{D}_2^{1/2}q$ as the edges spectrum.

For example, for the embryonic mouse data, we observe that the Harmonic decomposition has two eigenvalues close to zero. If we plot the harmonic values for these two eigenvectors in the vertices, we observe that they highlight the two major branches of the triangulated graph (Supp. Fig. S1C). This is equivalent to the spectral clustering algorithm, where spectra (and small eigenvalues) are associated with the number of disconnected components (or clusters) in a graph (Supp. Fig. S15).

4.6 Trajectory Embedding and Tree Inference

4.6.1 Trajectory Sampling

To generate trajectories, we sample paths (or edge flows) in the graph by following edges with positive divergence (or increasing pseudotime). Due to the sparsity of the triangulated graph $G^{(t)}$, we sample paths in $G^{(knn)}$. For this, we perform a preference random walk on graph $G^{(knn)}$. We choose a random starting point from vertices (cells) with m lowest pseudo-time values. We choose the next vertex randomly by considering the divergence values (w^s). Only positive divergences (increase in pseudo-time) are considered. We stop when no further positive potential is available. Next, we return to the triangulated graph $G^{(t)}$ and estimate shortest paths in case sampled edges (from $G^{(knn)}$) are not present in $G^{(t)}$. We define a path $\mathbf{f} \in \mathbb{R}^{\|\mathcal{E}^{(t)}\|}$ on a simplicial complex as:

$$\mathbf{f}[i,j] = \begin{cases} 1 & \text{if edge } (i,j) \text{ is traversed} \\ -1 & \text{if edge } (j,i) \text{ is traversed} \\ 0 & \text{otherwise} \end{cases} \tag{20}$$

Random walk is repeated n times. This provides us with a path matrix $\mathbf{F}^{(t)} \in \mathbb{R}^{\|\mathcal{E}^{(t)}\|\times n}$, where $\|\mathcal{E}^{(t)}\|$ is number of edges in graph $G^{(t)}$. See Supp. Fig. S1D for examples of sampled trajectories or edge flows.

4.6.2 Trajectory embedding and clustering

We next project these paths $\mathbf{F}^{(t)}$ onto harmonic space to estimate a trajectory embedding. Let's recapitulate the decomposition of the normalized Hodge 1-Laplacian (Eq.19):

$$\mathcal{L}_1 = \mathbf{U}\Lambda\mathbf{U}^{-1}, \tag{21}$$

where $\mathbf{U} = (\mathbf{u}_1, \cdots, \mathbf{u}_{\|\mathcal{E}^{(t)}\|})$ is the eigenvector matrix and $\Lambda = \mathrm{diag}(\lambda_1, \cdots, \lambda_{\|\mathcal{E}^{(t)}\|})$ are the eigenvectors. We assume the eigenvectors have been sorted by their corresponding increasing eigenvalues such that $0 \leq \lambda_1 \leq \lambda_2 \leq \cdots \leq \lambda_{\|\mathcal{E}^{(t)}\|}$.

Denote $\mathbf{H} := (\mathbf{u}_1, \cdots, \mathbf{u}_h)$ to be the matrix containing all the harmonic functions associated to $\mathcal{L}_1$, i.e. all of the eigenvectors corresponding to the 0 eigenvalues, where h is the number with eigenvalues being equal to 0 and $\mathbf{H} \in \mathbb{R}^{\|\mathcal{E}^{(t)}\| \times h}$. We further project edge flow matrix $\mathbf{F}^{(t)}$ onto the harmonic space by matrix multiplication such that

$$\mathbf{H}^{(t)} = \mathbf{H}^\top \mathbf{F}^{(t)} \tag{22}$$

where $\mathbf{H}^{(t)} \in \mathbb{R}^{htimesn}$ embed each trajectory into h dimensions. PHLOWER next performs clustering on $\mathbf{H}^{(t)}$ with DBSCAN[62] to group the paths into major differentiation trajectories. For the mouse embryonic cell data, we observe that the trajectory embedding (or trajectory map) reveals two clusters S1E (left) associated with the neuronal and myocyte differentiation.

4.6.3 Cumulative trajectory embedding and tree inference

The path representation presented in Eq. 20 do not keep the time step of a edge visit. Thus we also define a traversed edge flow (transversed path) matrix $\hat{\mathbf{f}} \in \mathbb{R}^{\|\mathcal{E}^{(t)}\| \times S}$ to record both the time step associated with every edge visit, i.e.:

$$\hat{\mathbf{f}}[i, j, s] = \begin{cases} 1 & \text{if edge } (i, j) \text{ is traversed in step } s \\ -1 & \text{if edge } (j, i) \text{ is traversed in step } s \\ 0 & \text{otherwise} \end{cases} \tag{23}$$

where S is the length of the flow, $1 \leq s \leq S$ is the sth step and $\|\mathcal{E}^{(t)}\|$ is number of edges in graph $G^{(t)}$. As we have n trajectories, we will have n traversed edge flow matrices $\{\hat{\mathbf{f}}_1, \hat{\mathbf{f}}_2, \cdots, \hat{\mathbf{f}}_n\}$.

We make use of cumulative trajectory embedding to represent paths and for the detection of major trajectories and branching points. For a path $\hat{\mathbf{f}}$, we can estimate a point associated with every step s in this cumulative trajectory embedding space as:

$$\mathbf{v}_s = \sum_{i=1}^{s} \mathbf{H}^\top \hat{\mathbf{f}}_{,i} \tag{24}$$

where $\hat{\mathbf{f}}_{,i} \in \mathbb{R}^{\|\mathcal{E}^{(t)}\|}$, $\mathbf{v}_s \in \mathbb{R}^h$ is a coordinate in cumulative trajectory embedding space associated to the sth step in trajectory $\hat{\mathbf{f}}$ and h is the number of harmonic functions. This is repeated for all step sizes, which defines a vector $\mathbf{v} = \{\mathbf{v}_1, \cdots, \mathbf{v}_S\}$ for every path. As observed in Supp. Fig. S1E, these vectors are low dimensional representations of paths in the cumulative trajectory embedding. By coloring paths from distinct groups with distinct colors, we can recognize branching point events, branches shared by trajectory groups and terminal branches. Note also that if we consider only the final entry for every path, we obtain the same result as in the previously described trajectory

embedding.

Recall that we have performed the DBSCAN clustering method to cluster the n paths into m groups $\{g_1, g_2, \cdots g_m\}$ on the trajectory embedding. PHLOWER next uses a procedure schematized in Supp. Fig. S17 to find the differentiation tree structure. First, it estimates pseudo-time values for every edge, i.e. the average pseudo-time u^s from vertices associated to the edge. It next bins all edges by considering their pseudo-time, i.e. it selects the trajectory group with the lowest pseudo-time and splits its edges in p bins (Supp. Fig. S17 B). The same range of pseuudo-time is used to bin all trajectory groups and bins are indexed in increasing pseudo-time (Supp. Fig. S17 C). After binning of edges for each group, PHLOWER next finds the branching points for all group pairs by comparing the distance of edges within the bin vs. the distance of edges between the bins for a given bin index i.

More formally, for groups g_i and g_j and bin k, their corresponding edges in cumulative space are defined as set $\mathbf{V}_i^k$, $\mathbf{V}_j^k$. We then estimate the average edge coordinate per bin to serve as backbones for every group, i.e.:

$$\overline{b_i^k} = \frac{1}{M} \sum_{v \in \mathbf{V}_i^k} v, \tag{25}$$

where $M = |\mathbf{V}_i^k|$ is the number of edges in the bin. We also consider the average distance between edges in a bin to have an estimate of the compactness of edges in a bin and trajectory, i.e.:

$$\overline{\sigma_i^k} = \frac{1}{M^2} \sum_{u \in \mathbf{V}_i^k} \sum_{v \in \mathbf{V}_i^k} \left\| u - v \right\|_2 \quad . \tag{26}$$

Finally, we calculate the distance between two groups g_i and g_j in time bin k, such that:

$$\mathrm{d}(i, j, k) = \left\| \frac{\overline{b_i^k}}{\overline{\sigma_i^k}} - \frac{\overline{b_j^k}}{\overline{\sigma_j^k}} \right\|_2 . \tag{27}$$

For every pair of groups, PHLOWER finds a unique branching point by transversing bins in decreasing order and finding the first bin such that $\mathrm{d}(i, j, k) < \sigma$ (as default 1).

This is repeated for all pairs of groups. The tree is finally built in a bottom up manner. PHLOWER first considers branching points with highest index and builds a sub-tree by merging the two trajectory groups at hand. This is repeated until all branching points are considered (Supp. Fig. S17D-E). PHLOWER finally defines the leaves and the root by finding more extreme points, edges with lowest and highest pseudo-time in a trajectory group. These are the so called milestones (branching points, root and end points) needed for evaluation by Dynverse[8]. Trajectories are redefined as branches, i.e. part of the trajectories between two milestones. We also allocate cells (vertices) to these branches. For this, we consider the location of all edges associated with a vertex and use the mean value in the cumulative trajectory embedding space. This is used to allocate cells to branches and to find the distance between respective milestones. Moreover, we provide this information for STREAM[5] for visualization as an STREAM tree.

4.6.4 Regulator and Marker Selection

We make use of the cumulative trajectory space and statistical tests to find markers and regulators associated to trajectories. Two compare two final branches, PHLOWER selects all cells associated within particular areas of the branches, i.e. highest 50% of the bins. Note that every cell can be visited by several edges. To consider this important information, we multiply expression count vector of each cell by the number of visits. We then perform a

statistical test (default is the $t-$test from scanpy[63]). In case we are interested in comparing sub-trees with several branches, PHLOWER first merges the sub-tree as a single branch, before the selection of the bin.

In the case of multimodal data (RNA and ATAC), PHLOWER also has a module to find regulators. First, we estimate a TF activity score per cell using chromVar[42]. We then use the previously described test to find branch specific regulators. Since TF activity cannot be discerned from TFs with similar motifs, we only consider genes, which TF activity is similar to the expression pattern at the selected branch as in[41]. We first get the average expression/TF activity of cells of bins around the branch of interest. We next smooth the gene expression using convolution (numpy.convolve)). We then estimate the correlation between gene expression and TF activity and use this to sort branch specific regulators.

4.7 Materials

4.7.1 Synthetic data sets

To test the power of PHLOWER in the detection of multiple branches trees, we generate 10 simulated data sets using diffusion-limited aggregation trees (DLA tree)[19] as proposed in PHATE[13]. For this, we use a Gaussian noise parameter of 5 and vary the parameter n_branch, which controls the number of branches in the trees, from 3 to 12. This generated trees with 5 to 18 branches. For every data, we generate 3000 points and 100 features. Of note, we use the same data as evaluated in PHATE as data with 10 branches. Next, we run PHATE to visualize the branches, with which we can future construct ground truth for dynverse benchmarking.

Next, we reformat this data to be used within the trajectory benchmarking framework dynverse[8] by using dynwrap. In short, dynverse needs detailed information of the branches, branch points and association of cells within a branch. To do so, we need to find the branching points of the DLA tree. First, we perform PHATE on the DLA high dimensional data to get embedding with 2 dimensions. We only consider embeddings, where the tree structure is preserved. Next, we find the branching points by finding 2 nearest neighbors of two branches. With these branching points, we created the branch backbones needed by dynverse. We calculate the association of each data point to a branching point (milestone percentage) by calculating the euclidean distance between the points related to each branch.

4.8 Benchmarking Evaluation

Dynverse includes wrappers for several trajectory methods. We explore the following methods in our evaluation: PAGA tree[4], monocle 3[20], slingshot[6], Slice[23], TSCAN[26], Slicer[27], MST[28] and Elpigraph[29]. We expand this by including a wrapper for STREAM[5] and PHLOWER. We first calculate the distance of each cell to all branches, next assign the cell to the nearest branch and use the distance ratio to associate cells to milestones. Next, we use dyneval to measure quality metrics for the generated trajectories. As in[8], we mainly focus on HIM(Hamming-Ipsen-Mikhailov distance) to measure the tree structure similarity; cor_{dist} to measure the correlation between the cell geodesic distances within predicted and true branches; $F1_{branches}$ and $F1_{milestones}$ to measure the accuracy of a cell assigned to the correct branches and the correct milestone (bifurcation points).

4.9 Kidney Organoids

4.9.1 Ethical statement

Permission for the creation and use of iPSCs in this study was obtained from the the ethical commission at RWTH Aachen University Hospital (approval number EK23-193).

Cell culture Generation of human iPSC-353 line: Erythroblasts from a healthy volunteer were reprogrammed using the CytoTune™-iPS 2.0 Sendai Reprogramming Kit (Thermo Fisher) according to the manufacturer's protocol. In short, erythroblasts were transduced using the CytoTune™-iPS 2.0 Sendai Reprogramming Kit and re-seeded on plates with inactivated MEFs to support the growth and pluripotency of iPSCs. Emerging iPSC colonies were picked, expanded and assessed for activation of stem cell markers to confirm pluripotency.

Generation of human induced pluripotent stem cell (iPSC) derived kidney organoids

Generation of human induced pluripotent stem cell (iPSC) derived kidney organoids iPSC were seeded using a density of 20,000 cells/cm2 on Geltrex (Thermo Fisher, Breda, the Netherlands) coated 6-well plates (Greiner Bio-one, Alphen aan de Rijn, the Netherlands). The differentiation protocol was based on our previous work[32]. In brief, differentiation towards ureteric bud-like and metanephric mesenchyme lineage was initiated using CHIR-99021 (10 μM, BioTechne Ltd., Abingdon, United Kingdom) in STEM™diff APEL™2 medium (StemCell Technologies, Cologne, Germany) for 3 and 5 days, respectively. Next, the medium was replaced sequentially for APEL™2 supplemented with fibroblast growth factor 9 (FGF9), 200 ng/ml, R&D systems) and heparin (1 μg/ml, Sigma-Aldrich, Zwijndrecht, Netherlands) up to day 7. On day 7, differentiated cells were trypsinized and mixed in a ratio of one part 3 days CHIR-differentiated cells and two parts 5 days CHIR-differentiated cells to stimulate crosstalk between both lineages in order to boost segmented nephrogenesis. To generate cell pellets, 300,000 cells per 1.5 ml tube were aliquoted from the cell mix and centrifuged 3 times at 300 rcf for 3 min changing position by 180° per cycle. Cell pellets were plated on Costar Transwell filters (type 3450, Corning, Sigma-Aldrich), followed by a one-hour CHIR pulse (5 μM) in APEL™2 medium added to the basolateral compartment. Next, medium was replaced for APEL™2 medium supplemented with FGF9 and heparin for additional 5 days and the entire 3D organoid culture was performed using the air-liquid interface. After 5 days of organoid culture, APEL™2 medium supplemented with human epidermal growth factor (hEGF, 10 ng/ml, Sigma-Aldrich). Medium was replaced every other day for an additional 13 days.

Silencing of ZIC2, RFX4 and PAX3 during stem cell-derived kidney organoid development

Kidney organoids were transfected using ON-TARGETplus™ SMARTpool siRNA's ZIC2 (Catnr L-017505-00-0005), RFX4 (catnr L-013577-00-0005) and PAX3 (Catnr L-012399-00-0005, work concentration 25nM, Horizon Discovery, Cambridge, UK) and DharmaFECT Transfection reagent 1 (0.5% v/v) from day 7+5 (intermediate mesoderm stage) onwards until the end of the protocol until day 7+18. Organoids were refreshed every other day.

RNA extraction, cDNA synthesis and qPCR

RNA from organoids was extracted using the PureLink RNA mini kit (Thermo Fisher) according to the manufacturer's protocol. RNA was stored at -80°C until further processing. cDNA synthesis was performed using 200 ng RNA as input, using the iScriptTM cDNA synthesis kit (Bio-rad) according to the manufacturer's protocol. The mRNA expression was quantified by performing a semi-quantitative real-time PCR using PowerUp SYBR Mastermix (Applied Biosystems) and primers targeting human RFX4, ZIC2, PAX3 genes (hZIC2_For AAAGGACCCA-CACAGGGGAGA, hZIC2_Rev GACGTGCATGTGCTTCTTCCT hRFX4_For TGGGAAGAGCATGCATTGTG hRFX4_Rev TCTTTCAATCCAGCTCTCTGTGG hPAX3_For GCAGTATGGACAAAGTGCCT hPAX3_Rev CAGGGCCAGTTTTAGCTCCA . After correction with the corresponding human GAPD gene (GAPDH_For GAAGGTGAAGGTCGGAGTCA, GAPDH_Rev TGGACTCCACGACGTACTCA), gene expression levels were plotted as fold change compared to control. For primer sequences please refer to the key resources table.

Harvesting kidney organoids for 10x genomics NEXT GEM multi-ome pipeline

To dissect nephrogenic differentiation trajectories in kidney organoids using the multiome pipeline, organoids were harvested at different time points during culture. The following differentiation stages were processed: day 7 (cells harvested from the 2D cell layer, primitive streak - intermediate mesoderm stage), organoids day 7+5 (day12), day 7+12 (day19) and day 7+18 (day25). These kidney organoid stages represent nephrogenesis ranging from intermediate mesoderm (day 7+5) towards metanephric mesenchyme and ureteric bud-like lineages (day 7+12) that result into nephron-like structures embedded by a (progenitor) stromal compartment at the end of the differentiation protocol (day 7+18). Kidney organoids were harvested on the respective dates (d7+5, d7+12, and d7+18) by cutting single organoids out of the transwell filter in a sterile flow hood using a scalpel. Organoids were washed with 5 ml PBS per filter at room temperature 3 times. Afterwards, single organoids were cut from the transwell filter with the organoids still being attached to the membrane, transferred to 1.7 ml cryovials (Greiner bio-one) and subsequently snap frozen and stored at -80°C until nuclei isolation.

Single nuclei isolation from kidney organoids

Snap frozen kidney organoids were thawed in PBS and crushed using a glass tube and douncer (Duran Wheaton Kimble Life Sciences, Wertheim/Main, Germany). After passing the single cell suspension through a 40 µm cell strainer (Greiner bio-one), the suspension was centrifuged at 4°C and 300xg for 5 min. Subsequently, the supernatant was discarded and the cell pellet was resuspended in Nuc101 cell lysis buffer (Thermo Fisher), supplemented with RNase and protease inhibitors (Recombinant RNase Inhibitor and Superase RNase Inhibitor, Thermo Fisher, and cOmplete Protease Inhibitor, Roche), incubated for 30 seconds and centrifuged at 4°C and 500xg for 5 min. After discarding the supernatant, the nuclei were carefully resuspended in PBS containing 1% (v/v) Ultra-Pure BSA (Invitrogen Ambion, Thermo Fisher) and Protector RNAse inhibitor (Sigma Aldrich). Single nuclei were counted using Trypan blue (Thermo Fisher) and prepared for 10x genomics ChromiumNextGEM Multiome pipeline v1 according to the manufacturers guidelines (https://cdn.10xgenomics.com/image/upload/v1666737555/support-documents/CG000338_ChromiumNextGEM_Multiome_ATAC_GEX_User_Guide_RevF.pdf).

FFPE tissue of human iPSC-derived kidney organoids

iPSC-derived kidney organoids were cut from the Transwell™ filter and fixated in 4% (v/v) formalin on ice for 20 min. Fixed iPSC-derived kidney organoids were stripped of the filter membrane using a scalpel. Each single organoid was embedded using 2.25% (w/v) agarose gel (Thermo Fisher). After embedding for 5 min at 4∘C, the iPSC-derived kidney organoids were transferred to embedding cassettes and paraffinized. After paraffinization, iPSC-derived kidney organoids were cut at a thickness of 4 μm using a rotary microtome (Microm HM355 S, GMI) and mounted on FLEX IHC microscope slides (DAKO, Agilent Technologies) for immunofluorescence staining or Xenium array slides for spatial analysis.

Immunofluorescence staining

Slides were deparaffinized using series of xylol ($2^{\times}$) and 100% (v/v) ethanol ($3^{\times}$), followed by antigen retrieval by boiling slides in Tris-buffered EDTA (VWR Chemicals) for 20 minutes. Primary (1:100) and secondary (1:200) antibodies were diluted in PBS containing 1% (v/v) bovine serum albumin (BSA; Sigma-Aldrich). Primary antibodies (NPHS1, AF 4269-SP, RD Systems, Vimentin, ab92547, Abcam) were incubated overnight at 4°C, and secondary antibodies were incubated at RT for 2 h (donkey anti-sheep IgG (H+L) alexa fluor 647 (ThermoFisher), donkey

anti-rabbit IgG (H+L) alexa fluor 488 (ThermoFisher), DAPI (300nM,

4.10 4',6-Diamidine-2'-phenylindole dihydrochloride

Merck). After each antibody incubation, slides were washed three times in PBS for 5 min. Slides were mounted using Fluoromount-G® (Southern Biotech, SanBio). Images were captured using a Zeiss LSM 980 confocal microscope.

4.10.1 Computational Analysis of Kidney Organoids

After read mapping using the cellranger-arc tool(version 1.0.1), we filter the low-quality cells using information both from scRNA and scATAC reads. We first import scRNA to Seurat[64] to get the scRNA metrics for filtering. We next import the fragments into ArchR[65] to get the scATAC metrics for filtering. With the information above, we retain cells with barcodes in both scRNA and scATAC count matrices. Next, we filter the cells using threshold nFeatureRNA > 200 & nCountRNA <400,000 &percent.mito > 5 and scATAC using thresholds in ArchR that minTSS = 6 & minFrags = 2500 & maxFrags = 1e+05. We next perform preprocessing to scRNA using Seurat, to do this, we first normalize the scRNA data by calling NormalizeData with the default parameters, next we find top variable features with parameter selection.method='vst'. Next, we scale the data by regressing out the cell cycle and mitochondrial effect. We next run PCA with 50 PCs. To remove the batch effects, we next run harmony[33] to integrate the four samples. For scATAC data, we use ArchR to perform the preprocessing. We first create Arrow files using the filter threshold aforementioned by calling createArrowFiles, the tile matrices are created directly from the fragment files. Next, we add doublets score by calling addDoubletScores for each sample followed by function filterDoublets to remove doublets with default parameters. Next, we run addIterativeLSI on the tile matrices to add dimensional reductions. A batch correction is also called using Harmony[33] with function addHarmony. To obtain a uniform dimension reduction for the downstream analysis, we next run MOJITOO[9] to integrate the scRNA and scATAC data with default parameters.

MOJITOO embedding was used as input for PHLOWER. An important parameter is the indication of the root cells. For this, we performed a clustering analysis using Seurat[64] with resolution=2.5 on the MOJITOO embedding space. The root cells were defined by clusters predominantly present in day 7 and with the expression of mesoderm markers (TBXT, MESP1, KDR5). PHLOWER found 28 dimensions with zero eigenvalues and clustering analysis of the trajectory space detected 16 groups. We removed 4 main trajectories outliers (less than 0.5% samples inner the cluster) and one trajectory, where cells had a low pseudotime values (e.g. they did not differentiate). Finally, some clusters had the same end time points. We therefore keep the one with the largest number of trajectories. This resulted in the 9 final trajectories found by PHLOWER.

4.10.2 Computational Analysis of Xenium Experiments of Kidney Organoids

To select markers, we used the phlower.tl.tree_mbranch_markers function to identify markers for each main branch (stromal, neuronal, tubular and podocytes), focusing on cells with highest pseudotime according to PHLOWER (top 50%). Next, we further selected markers with expression specific to sub-branches (tubular, podocytes, stromal 1, stromal 2-4, neuron 1, and neuron 2-3). For this, we retained only genes with a padj < 0.05 and logFC > 1.5 for the main branch markers. Next, we only considered protein-coding genes according to Ensembl (Version GRCh38.104). We then scaled the logFC values of both main and sub-branches to a 0-1 range and calculated the mean normalized logFC for each branch and its sub-branches. We selected the top 12 genes for each sub-branch based on the mean normalized logFC. For TF selection, we used TF-Gene correlation along each sub-branch to identify 5 TFs per main branch using scMEGA analysis shown in Supp. Fig. S8. Additionally, we included literature based cell type markers

reported in Supp. Fig. S6, which supported the annotation of the multiome single cell data. In total, we identified 100 genes for the Xenium experiment (see Supp. Table S1). The panel primers were designed with the Xenium Panel Designer tool provided by 10X Genomics.

For the data analysis, we used Xenium Explore3 to inspect each region and remove those that did not show differentiation and remove stromal cell patches around organoid edges. This process left us with two scrambled siRNA regions, one siRNA region, one day 19 region, and two day 25 regions. Note that multiple regions corresponds to distinct sections of the same organoid. Next, we used Space Ranger with default parameters and loaded each Xenium sample using Seurat (version 5.0.2) with the LoadXenium function and removed cells based on the organoid masks. We integrated all cells using Seurat's merge function and filtered out cells with zero nCount_Xenium. We next applied SCTransform for data normalization. PCA for dimensionality reduction and Louvain cluster (50 PCs and resolution = 0.3); and estimated a UMAP for visualisation. Next, we annotated the clusters by examining the gene expression of known cell type markers. We excluded 5 clusters with 33,396 cells due to low nFeature_Xenium(<20) and nCount_Xenium (<60). This potentially represents cells, whose markers are not present in our panel.

For the day 19 and day 25 regions, we performed trajectory inference using PHLOWER using a subset of the cells (2000 per cluster). We used Mesoderm cells as the root for the trajectory inference and identified three end branches. Finally, we integrated PHLOWER with STREAM for visualization.

Code and data availability

Code, documentation and examples for running analysis of this manuscript are available on github https://github.com/CostaLab/phlo and readthedocs https://phlower.readthedocs.io/en/latest/. Data objects with the kidney organoid (multiome and Xenium) as well as the benchmarking data have be deposited in zenodo.

Acknowledgements

This project has been funded by the German Research Foundation (DFG) (3888802535, CRU344- 417911533 and CRU5011 - 445703531) and the Consortia E:MED Fibromap and CureFib funded by the German Ministry of Education and Science (BMBF). This work was further supported by grants of the German Research Foundation (DFG: SFBTRR219 322900939, CRU344- 4288578857858, CRU5011- 445703531), by a grant of the European Research Council (ERC-COG 101043403), the Dutch Kidney Foundation (DKF), TASKFORCE EP1805 and the NWO VIDI 09150172010072.

Competing interests

The authors declare no competing interests.

References

1. Kim, J., Koo, B. K. & Knoblich, J. A. Human organoids: model systems for human biology and medicine. *Nat. Rev. Mol. Cell Biol.* **21**, 571–584, DOI: 10.1038/s41580-020-0259-3 (2020).
2. Ma, S. *et al.* Chromatin Potential Identified by Shared Single-Cell Profiling of RNA and Chromatin. *Cell* **183**, 1103–1116.e20, DOI: 10.1016/j.cell.2020.09.056 (2020).
3. Costa, I. G. Dissecting gene regulation with multimodal sequencing. *Nat. Methods* DOI: 10.1038/s41592-023-01957-1 (2023).

4. Wolf, F. A. *et al.* Paga: graph abstraction reconciles clustering with trajectory inference through a topology preserving map of single cells. *Genome biology* **20**, 1–9 (2019).

5. Chen, H. *et al.* Single-cell trajectories reconstruction, exploration and mapping of omics data with stream. *Nat. communications* **10**, 1903 (2019).

6. Street, K. *et al.* Slingshot: cell lineage and pseudotime inference for single-cell transcriptomics. *BMC genomics* **19**, 1–16 (2018).

7. Lynch, A. W. *et al.* MIRA: joint regulatory modeling of multimodal expression and chromatin accessibility in single cells. *Nat. Methods* **19**, 1097–1108, DOI: 10.1038/s41592-022-01595-z (2022).

8. Saelens, W., Cannoodt, R., Todorov, H. & Saeys, Y. A comparison of single-cell trajectory inference methods. *Nat. biotechnology* **37**, 547–554 (2019).

9. Cheng, M., Li, Z. & Costa, I. G. MOJITOO: a fast and universal method for integration of multimodal single-cell data. *Bioinformatics* **38**, i282–i289, DOI: 10.1093/bioinformatics/btac220 (2022). https://academic.oup.com/bioinformatics/article-pdf/38/Supplement_1/i282/44269504/btac220.pdf.

10. Tewari, A. *et al.* Mofa: Model-based deep convolutional face autoencoder for unsupervised monocular reconstruction. In *Proceedings of the IEEE International Conference on Computer Vision Workshops*, 1274–1283 (2017).

11. Coifman, R. R. *et al.* Geometric diffusions as a tool for harmonic analysis and structure definition of data: Diffusion maps. *Proc. national academy sciences* **102**, 7426–7431 (2005).

12. Haghverdi, L., Buettner, F. & Theis, F. J. Diffusion maps for high-dimensional single-cell analysis of differentiation data. *Bioinformatics* **31**, 2989–2998 (2015).

13. Moon, K. R. *et al.* Phate: a dimensionality reduction method for visualizing trajectory structures in high-dimensional biological data. *BioRxiv* **120378** (2017).

14. Schaub, M. T., Benson, A. R., Horn, P., Lippner, G. & Jadbabaie, A. Random Walks on Simplicial Complexes and the Normalized Hodge 1-Laplacian. *SIAM Rev.* **62**, 353–391, DOI: 10.1137/18M1201019 (2020).

15. Von Luxburg, U. A tutorial on spectral clustering. *Stat. computing* **17**, 395–416 (2007).

16. Frantzen, F., Seby, J.-B. & Schaub, M. T. Outlier detection for trajectories via flow-embeddings. In *2021 55th Asilomar Conference on Signals, Systems, and Computers*, 1568–1572 (IEEE, 2021).

17. Gansner, E. R., Koren, Y. & North, S. Graph drawing by stress majorization. In *International Symposium on Graph Drawing*, 239–250 (Springer, 2004).

18. Treutlein, B. *et al.* Dissecting direct reprogramming from fibroblast to neuron using single-cell rna-seq. *Nature* **534**, 391–395 (2016).

19. Witten Jr, T. A. & Sander, L. M. Diffusion-limited aggregation, a kinetic critical phenomenon. *Phys. review letters* **47**, 1400 (1981).

20. Cao, J. *et al.* The single-cell transcriptional landscape of mammalian organogenesis. *Nature* **566**, 496–502 (2019).

21. duVerle, D. A., Yotsukura, S., Nomura, S., Aburatani, H. & Tsuda, K. Celltree: an r/bioconductor package to infer the hierarchical structure of cell populations from single-cell rna-seq data. *BMC bioinformatics* **17**, 1–17 (2016).

22. Herring, C. A. *et al.* Unsupervised trajectory analysis of single-cell rna-seq and imaging data reveals alternative tuft cell origins in the gut. *Cell systems* **6**, 37–51 (2018).

23. Guo, M., Bao, E. L., Wagner, M., Whitsett, J. A. & Xu, Y. Slice: determining cell differentiation and lineage based on single cell entropy. *Nucleic acids research* **45**, e54–e54 (2017).

24. Grün, D. *et al.* Single-cell messenger rna sequencing reveals rare intestinal cell types. *Nature* **525**, 251–255 (2015).

25. Grün, D. *et al.* De novo prediction of stem cell identity using single-cell transcriptome data. *Cell stem cell* **19**, 266–277 (2016).

26. Ji, Z. & Ji, H. Tscan: Pseudo-time reconstruction and evaluation in single-cell rna-seq analysis. *Nucleic acids research* **44**, e117–e117 (2016).

27. Welch, J. D., Hartemink, A. J. & Prins, J. F. Slicer: inferring branched, nonlinear cellular trajectories from single cell rna-seq data. *Genome biology* **17**, 1–15 (2016).

28. Graham, R. L. & Hell, P. On the history of the minimum spanning tree problem. *Annals Hist. Comput.* **7**, 43–57 (1985).

29. Albergante, L. *et al.* Robust and scalable learning of complex intrinsic dataset geometry via elpigraph. *Entropy* **22**, 296 (2020).

30. Saelens, W., Cannoodt, R., Todorov, H. & Saeys, Y. A comparison of single-cell trajectory inference methods. *Nat. Biotechnol.* **37**, 547–554, DOI: 10.1038/s41587-019-0071-9 (2019).

31. Setty, M. *et al.* Characterization of cell fate probabilities in single-cell data with Palantir. *Nat. Biotechnol.* **37**, 451–460, DOI: 10.1038/s41587-019-0068-4 (2019).

32. Jansen, J. *et al.* Sars-cov-2 infects the human kidney and drives fibrosis in kidney organoids. *Cell Stem Cell* **29**, 217–231 (2022).

33. Korsunsky, I. *et al.* Fast, sensitive and accurate integration of single-cell data with harmony. *Nat. methods* **16**, 1289–1296 (2019).

34. Schmidt-Ott, K. M. How to grow a kidney: patient-specific kidney organoids come of age. *Nephrol. Dial. Transplantation* **32**, 17–23, DOI: 10.1093/ndt/gfw256 (2016). https://academic.oup.com/ndt/article-pdf/32/1/17/9675162/gfw256.pdf.

35. Evseenko, D. *et al.* Mapping the first stages of mesoderm commitment during differentiation of human embryonic stem cells. *Proc. Natl. Acad. Sci.* **107**, 13742–13747 (2010).

36. Menon, R. *et al.* Single-cell analysis of progenitor cell dynamics and lineage specification in the human fetal kidney. *Development* **145**, dev164038, DOI: 10.1242/dev.164038 (2018). https://journals.biologists.com/dev/article-pdf/145/16/dev164038/1853282/dev164038.pdf.

37. Hochane, M. *et al.* Single-cell transcriptomics reveals gene expression dynamics of human fetal kidney development. *PLOS Biol.* **17**, 1–31, DOI: 10.1371/journal.pbio.3000152 (2019).

38. Combes, A. N. *et al.* Single cell analysis of the developing mouse kidney provides deeper insight into marker gene expression and ligand-receptor crosstalk. *Development* **146**, dev178673, DOI: 10.1242/dev.178673 (2019). https://journals.biologists.com/dev/article-pdf/146/12/dev178673/3112612/dev178673.pdf.

39. Wu, H. *et al.* Comparative analysis and refinement of human psc-derived kidney organoid differentiation with single-cell transcriptomics. *Cell stem cell* **23**, 869–881 (2018).

40. Subramanian, A. *et al.* Single cell census of human kidney organoids shows reproducibility and diminished off-target cells after transplantation. *Nat. communications* **10**, 5462 (2019).

41. Li, Z., Nagai, J. S., Kuppe, C., Kramann, R. & Costa, I. G. scmega: single-cell multi-omic enhancer-based gene regulatory network inference. *Bioinforma. Adv.* **3**, vbad003 (2023).

42. Schep, A. N., Wu, B., Buenrostro, J. D. & Greenleaf, W. J. chromvar: inferring transcription-factor-associated accessibility from single-cell epigenomic data. *Nat. methods* **14**, 975–978 (2017).

43. Kann, M. *et al.* Genome-wide analysis of wilms' tumor 1-controlled gene expression in podocytes reveals key regulatory mechanisms. *J. Am. Soc. Nephrol. JASN* **26**, 2097 (2015).

44. Schreibing, F. & Kramann, R. Mapping the human kidney using single-cell genomics. *Nat. Rev. Nephrol.* **18**, 347–360 (2022).

45. Kompatscher, A. *et al.* Loss of transcriptional activation of the potassium channel kir5. 1 by hnf1β drives autosomal dominant tubulointerstitial kidney disease. *Kidney international* **92**, 1145–1156 (2017).

46. Aue, A. *et al.* A grainyhead-like 2/ovo-like 2 pathway regulates renal epithelial barrier function and lumen expansion. *J. Am. Soc. Nephrol. JASN* **26**, 2704 (2015).

47. García-Palmero, I. *et al.* Twist1-induced activation of human fibroblasts promotes matrix stiffness by upregulating palladin and collagen a1(VI). *Oncogene* **35**, 5224–5236 (2016).

48. Kawane, T. *et al.* Runx2 is required for the proliferation of osteoblast progenitors and induces proliferation by regulating Fgfr2 and Fgfr3. *Sci. Rep.* **8**, 13551 (2018).

49. Terzić, J. & Saraga-Babić, M. Expression pattern of PAX3 and PAX6 genes during human embryogenesis. *Int. J. Dev. Biol.* **43**, 501–508 (1999).

50. Nagai, T. *et al.* Zic2 regulates the kinetics of neurulation. *Proc. Natl. Acad. Sci. U. S. A.* **97**, 1618–1623 (2000).

51. Zhang, D., Zeldin, D. C. & Blackshear, P. J. Regulatory factor X4 variant 3: a transcription factor involved in brain development and disease. *J. Neurosci. Res.* **85**, 3515–3522 (2007).

52. Janesick, A. *et al.* High resolution mapping of the tumor microenvironment using integrated single-cell, spatial and in situ analysis. *Nat. Commun.* **14**, 8353 (2023).

53. Sriramkumar, S. *et al.* Single-cell analysis of a high-grade serous ovarian cancer cell line reveals transcriptomic changes and cell subpopulations sensitive to epigenetic combination treatment. *Plos one* **17**, e0271584 (2022).

54. Safi, W. *et al.* Assessing kidney development and disease using kidney organoids and crispr engineering. *Front. Cell Dev. Biol.* **10**, 948395 (2022).

55. Serrano, A., Berthelet, J., Naik, S. H. & Merino, D. Mastering the use of cellular barcoding to explore cancer heterogeneity. *Nat. Rev. Cancer* **22**, 609–624 (2022).

56. Maehara, K. & Ohkawa, Y. Modeling latent flows on single-cell data using the hodge decomposition. *bioRxiv* 592089 (2019).

57. Zelnik-Manor, L. & Perona, P. Self-tuning spectral clustering. *Adv. neural information processing systems* **17** (2004).

58. Delvenne, J.-C., Yaliraki, S. N. & Barahona, M. Stability of graph communities across time scales. *Proc. national academy sciences* **107**, 12755–12760 (2010).

59. Ortmann, M., Klimenta, M. & Brandes, U. A sparse stress model. In *International Symposium on Graph Drawing and Network Visualization*, 18–32 (Springer, 2016).

60. Delaunay, B., Vide, S., Lamémoire, A. & De Georges, V. Bulletin de l'academie des sciences de l'urss. *Cl. des sciences mathématiques et naturelles* **6**, 793–800 (1934).

61. Schaub, M. T., Zhu, Y., Seby, J.-B., Roddenberry, T. M. & Segarra, S. Signal processing on higher-order networks: Livin'on the edge... and beyond. *Signal Process.* **187**, 108149 (2021).

62. Ester, M., Kriegel, H.-P., Sander, J., Xu, X. *et al.* A density-based algorithm for discovering clusters in large spatial databases with noise. In *kdd*, vol. 96, 226–231 (1996).

63. Wolf, F. A., Angerer, P. & Theis, F. J. Scanpy: large-scale single-cell gene expression data analysis. *Genome biology* **19**, 1–5 (2018).

64. Stuart, T. *et al.* Comprehensive integration of single-cell data. *Cell* **177**, 1888–1902 (2019).

65. Granja, J. M. *et al.* Archr is a scalable software package for integrative single-cell chromatin accessibility analysis. *Nat. genetics* **53**, 403–411 (2021).

5 Supplement

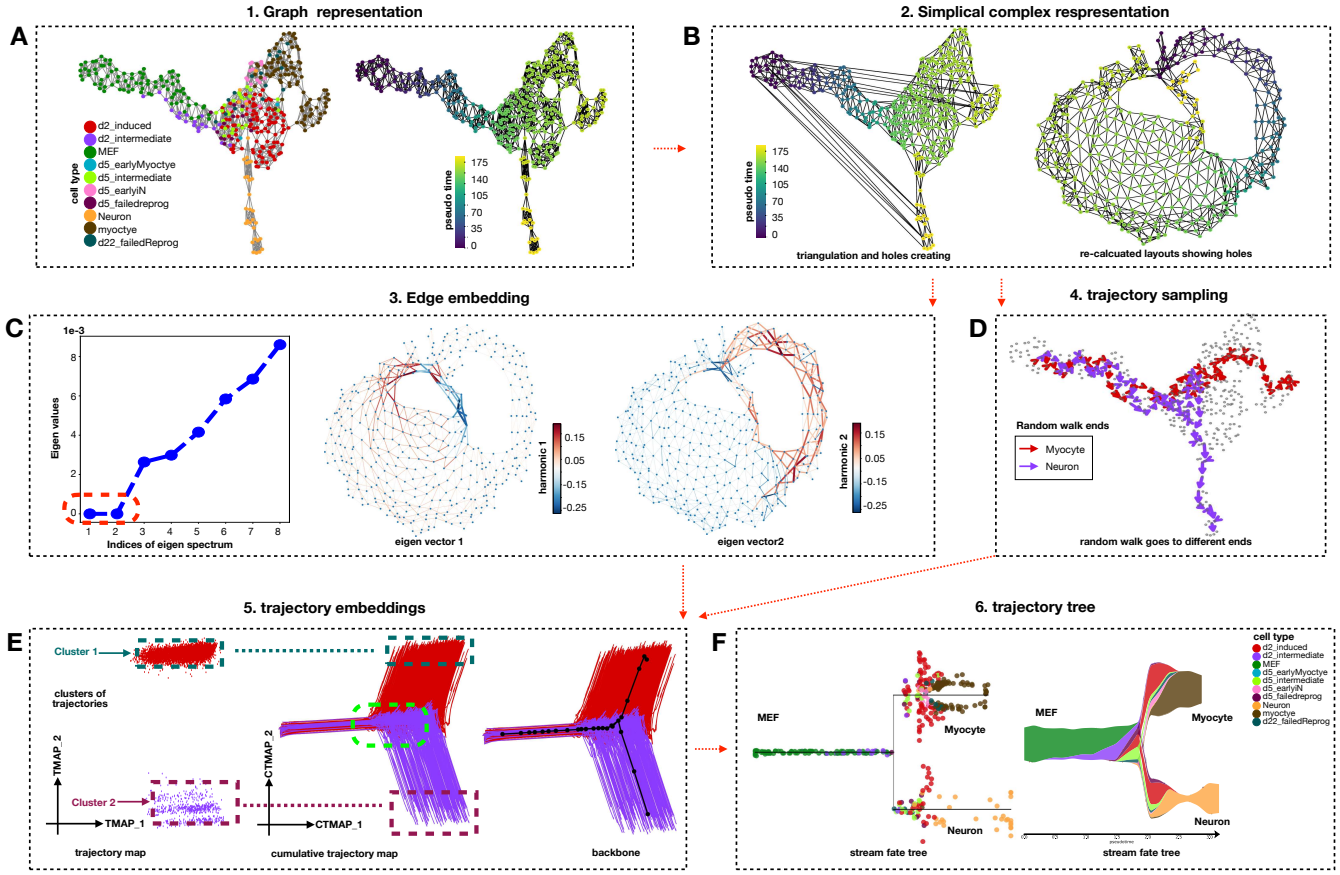

Figure S1. Detailed steps of PHLOWER on a single cell data with mouse embryonic fibroblasts towards neurons and myocytes A) First, PHLOWER estimates a graph representation using kernels and stress majorization layout[17]. Colors correspond to cluster labels as defined in[18]. This information (labels) is not used by PHLOWER algorithms B) Next, a pseudo-time is estimated using the zero-order Laplacian and using MEF cluster as root. The definition of a root is the only supervision required in PHLOWER. Edges between cells are obtained via Delaunay triangulation (left). To create holes in the simplicial complex, PHLOWER performs a trick by including edges between high pseudo-time towards low pseudo time vertices (middle). If we re-run the graph layout, two holes are clearly visible in the graph. C) PHLOWER next performs the spectral decomposition of the Hodge Laplacian of the simplicial complex. This indicates two zero eigenvalues (or holes). By plotting eigenvector values on the edges, we observe that the first eigenvector discriminates edges in the neuronal branch vs. others, while the second eigenvector discriminates the myocyte related cells from others. D) Next, PHLOWER generates trajectories by random walk on the simplicial complex representation to obtain edge-flow vectors. E) Finally, PHLOWER creates a trajectory embedding by a dot product of the edge flows with the harmonic decomposition. We observe two clear clusters in the trajectory map (left), which are detected by providing this embedding as input for DBSCAN[62]. We can similarly create a cumulative trajectory map by creating edge flows of trajectories by considering only the first one, two, three and so on first differentiation events. PHLOWER uses this space to delineate the backbones of differentiation trajectories and to detect branching points events (in green, right panel). F) PHLOWER outputs a differentiation tree, pseudo-time values and an allocation of cells to positions in the branches. PHLOWER makes use of STREAM to visualise the final trajectories.

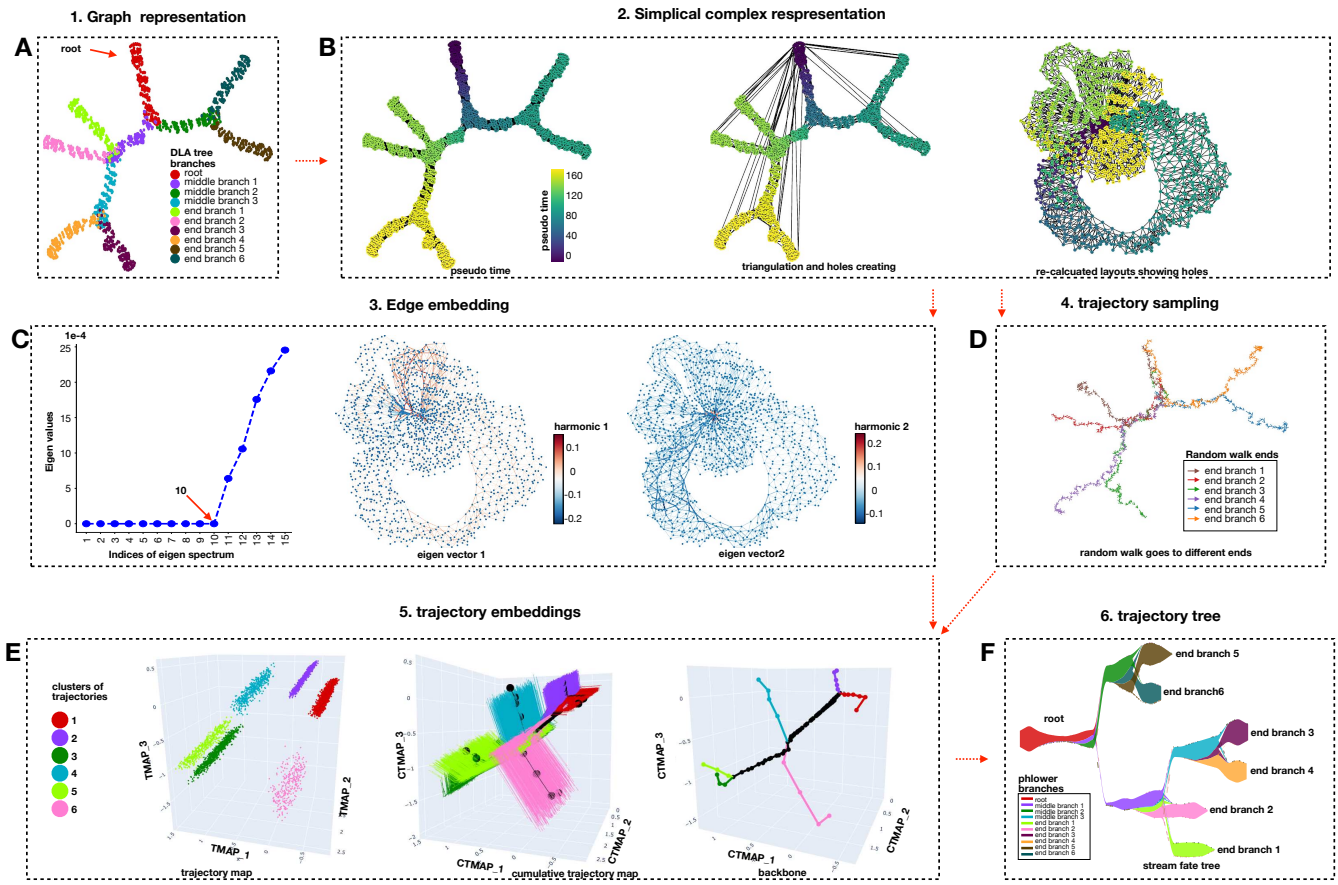

Figure S2. PHLOWER workflow for the simulated tree dataset with 10 total branches Panels A-F show distinct PHLOWER estimates for the simulated data with 10 branches exactly as described in Supp. Fig. S1. Note that in this complex multi-branched data, the 2 dimensional representation of the graph layout of the simplicial complex (B) can not capture the data complexity and does not properly display all the holes. Clustering analysis in the trajectory embedding detects the six main trajectories present in the data (E) and recovers an almost perfect differentiation tree (F). Of note, the number of zero-eigenvalues (10) is higher than the number of main trajectories (6). This is potentially due to small (and noise associated) holes in the graph. This do not impact the precision of the clustering analysis to find the correct branches.

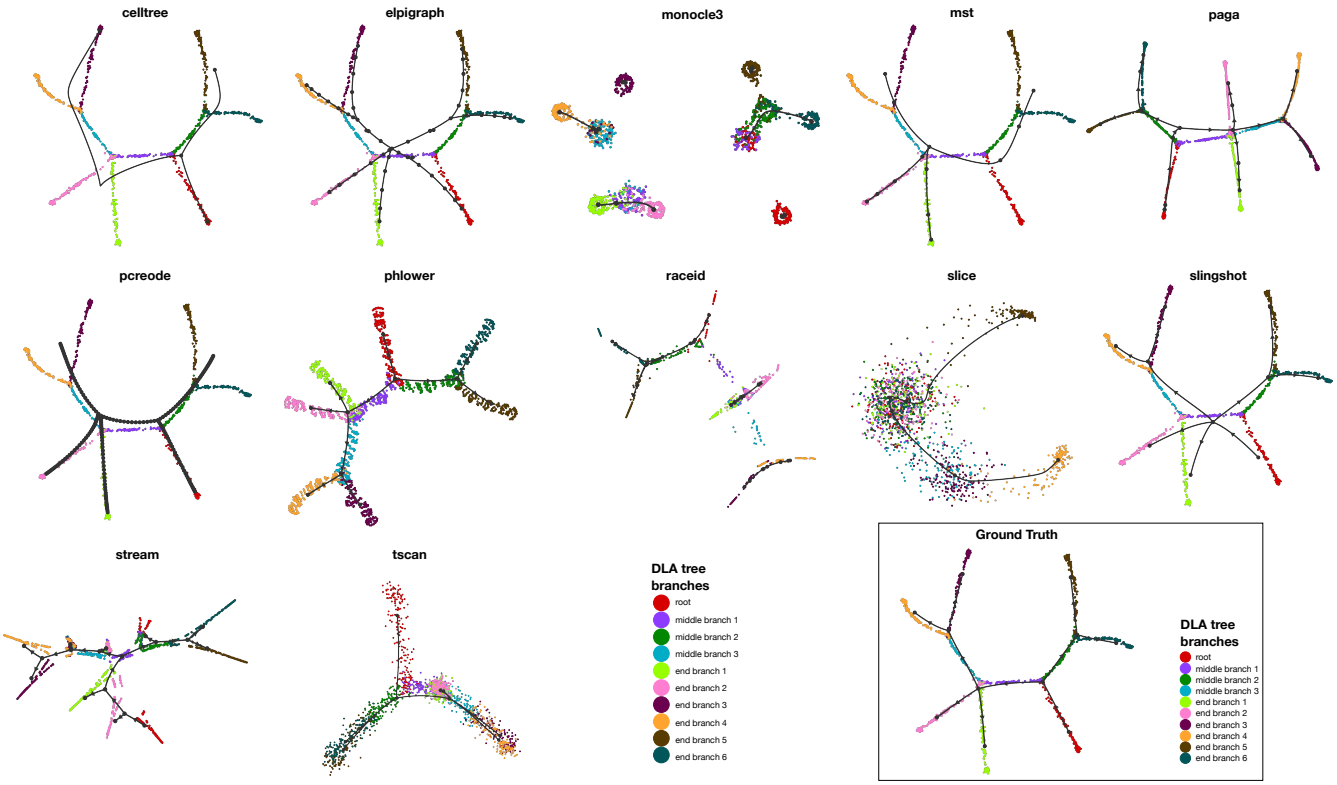

Figure S3. Differentiation tree backbones in the simulated data with 10 branches. We show embedding and trees for the ground truth and 12 evaluated algorithms for the data with 10 branches. This data has a root branch, three intermediary branches and six end branches. The colors of cells represent the true labels of branches. Embedings represent the default as provided by the algorithm. As this is not provided by celltree, elpigraph, mst, preode and slingshot, we used the embedding produced by PHATE[13]. The same embeding was used to show the ground truth. Slicer results are not shown as it failed to run in this data.

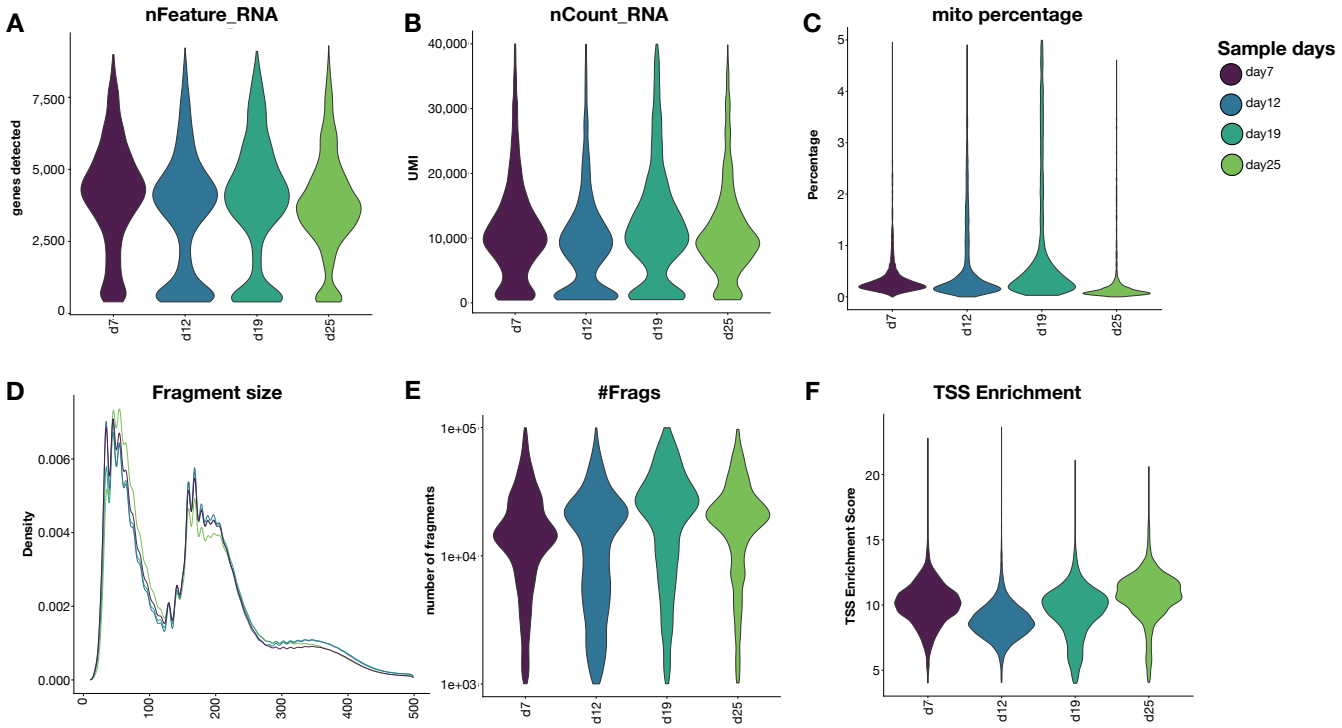

Figure S4. Quality check for kidney organoids single cell data. We show violin plots with quality check information after filtering and cell detection. These are: (A) number of features (genes) in RNA, (B) number of counts (transcripts) in RNA, (C) proportion of mitochondrial genes (RNA), (D) fragment sizes distribution (ATAC), (E) number of fragments (ATAC) and (F) transcription start site enrichment. All libraries had similar values across days of sampling.

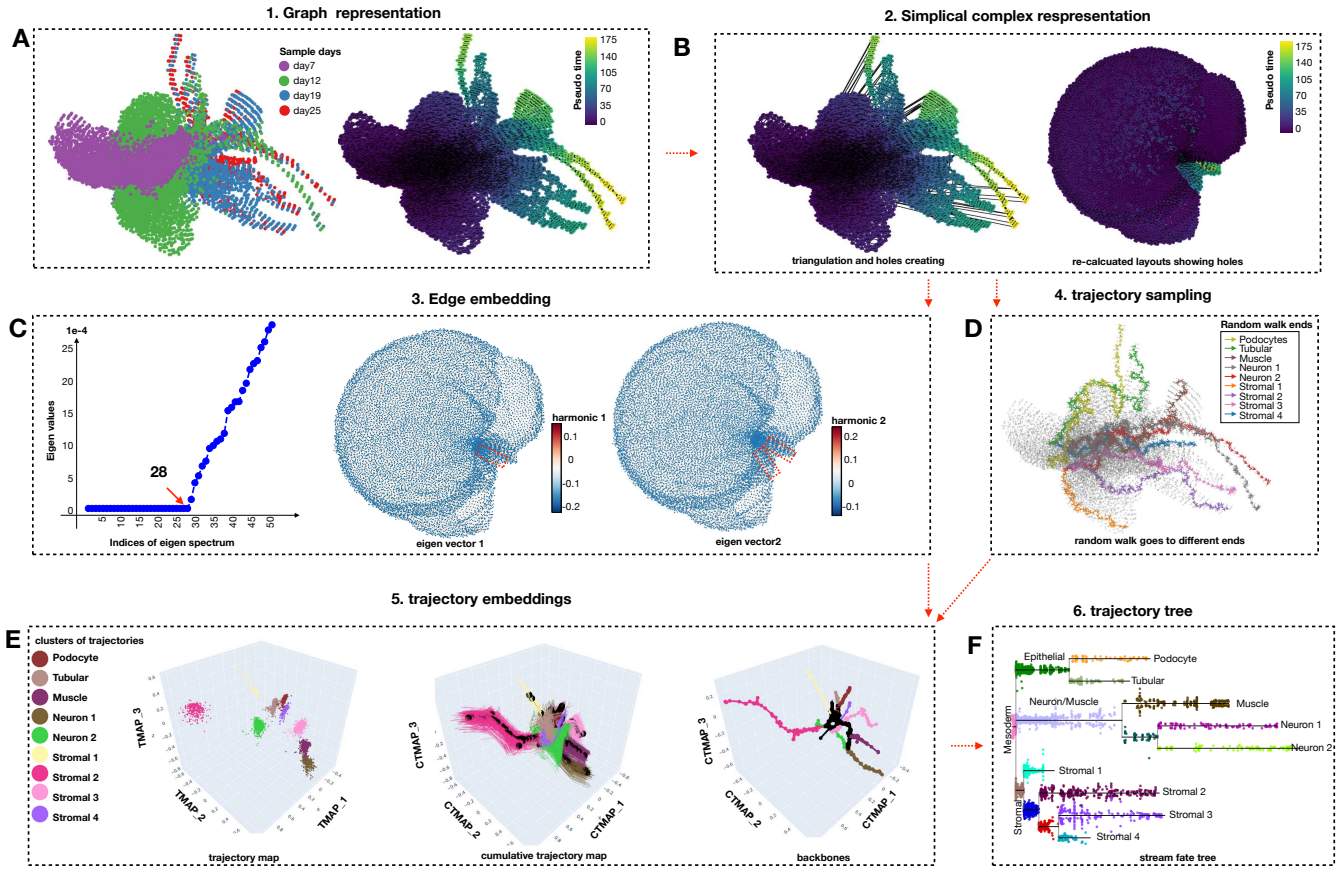

Figure S5. PHLOWER workflow for the kidney organoids data Panels A-F are obtained as described in Supp. Fig. S1.

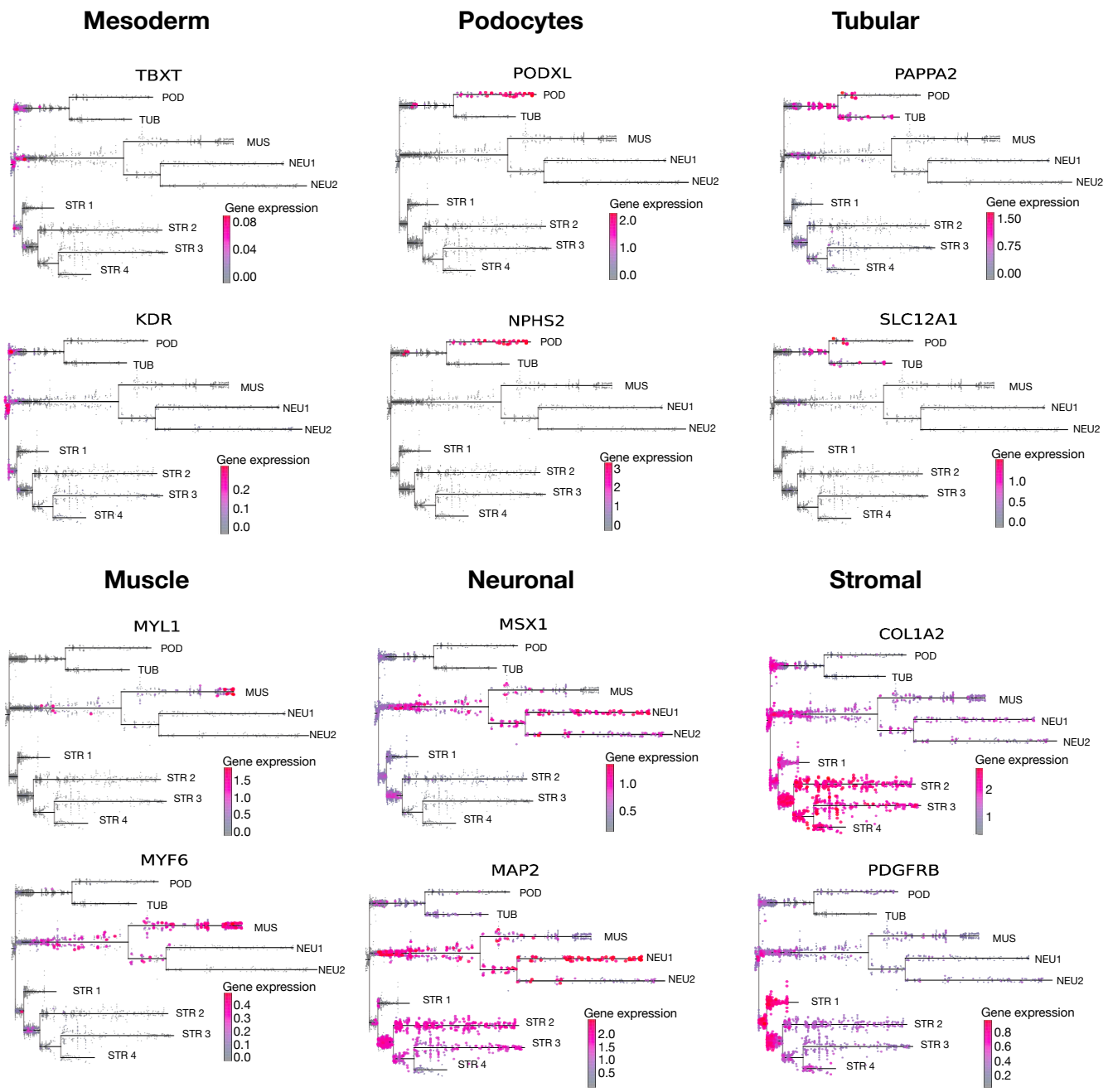

Figure S6. Gene markers for cell type of PHLOWER tree identification. A) Expressions of the gene markers TBXT, KDR, PODXL, NPHS2, PAPPA2, SLC12A1, MYL1, MYF6, MSX1, MAP2, COL1A2 and PDGFRB are shown in the PHLOWER tree (same genes as in Fig.3D).

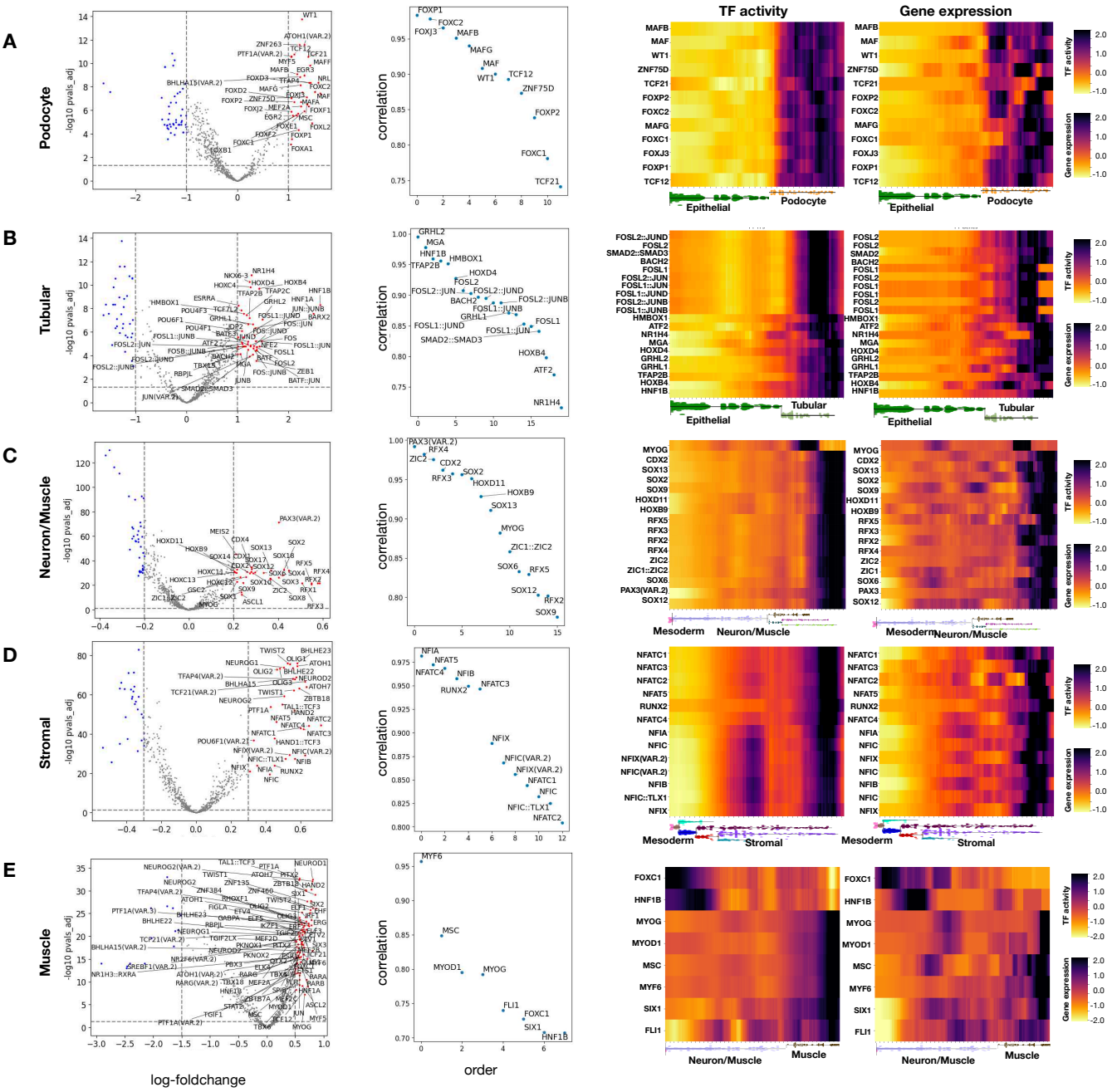

Figure S7. Regulators associated with cell branches. A) Regulators associated with Podocyte cells. We perform a differential expression analysis to find genes specific to podocytes (comparing with tubular cells) (left). Of these DE genes, we select transcription factors, which transcription factor activity (scATAC-seq), is highly correlated with gene expression (middle). Heatmaps display the TF activity and gene expression profiles of these TFs over the differentiation path from mesoderm towards podocyte cells. **B)** Same as (A) when contrasting tubular cells with podocytes. **C)** Sames as (A) when contrasting neuronal/muscle cells with all other branches. **D)** Same as (A) when contrasting stromal cells with all other branches. **E)** Same as (A) when contrasting Muscle cells with all other Neuron cells.

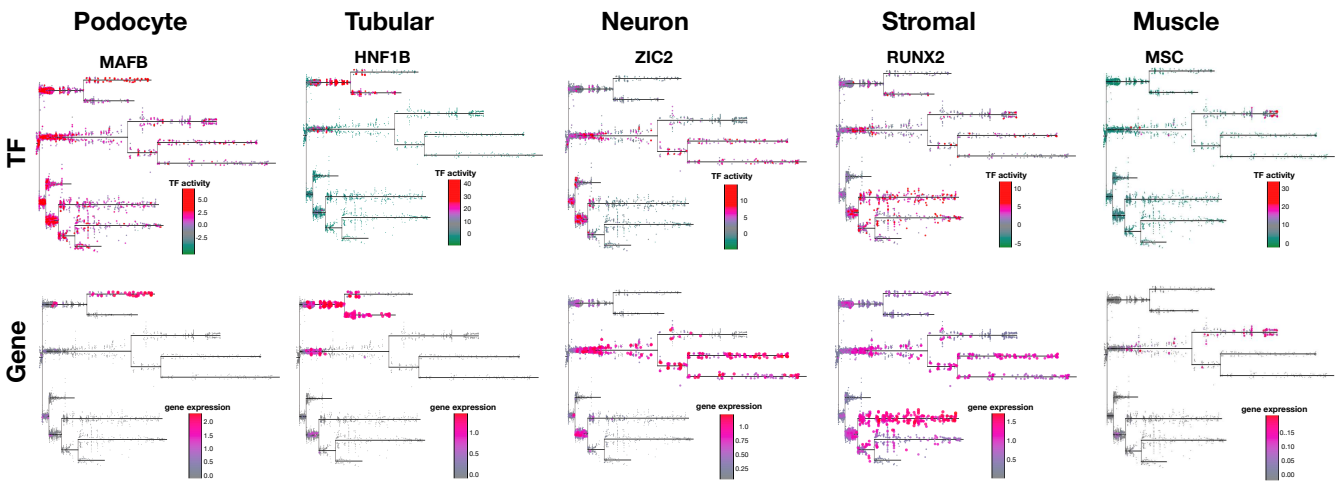

Figure S8. TF activity and gene expression showing in the PHLOWER estimated differentiation tree.

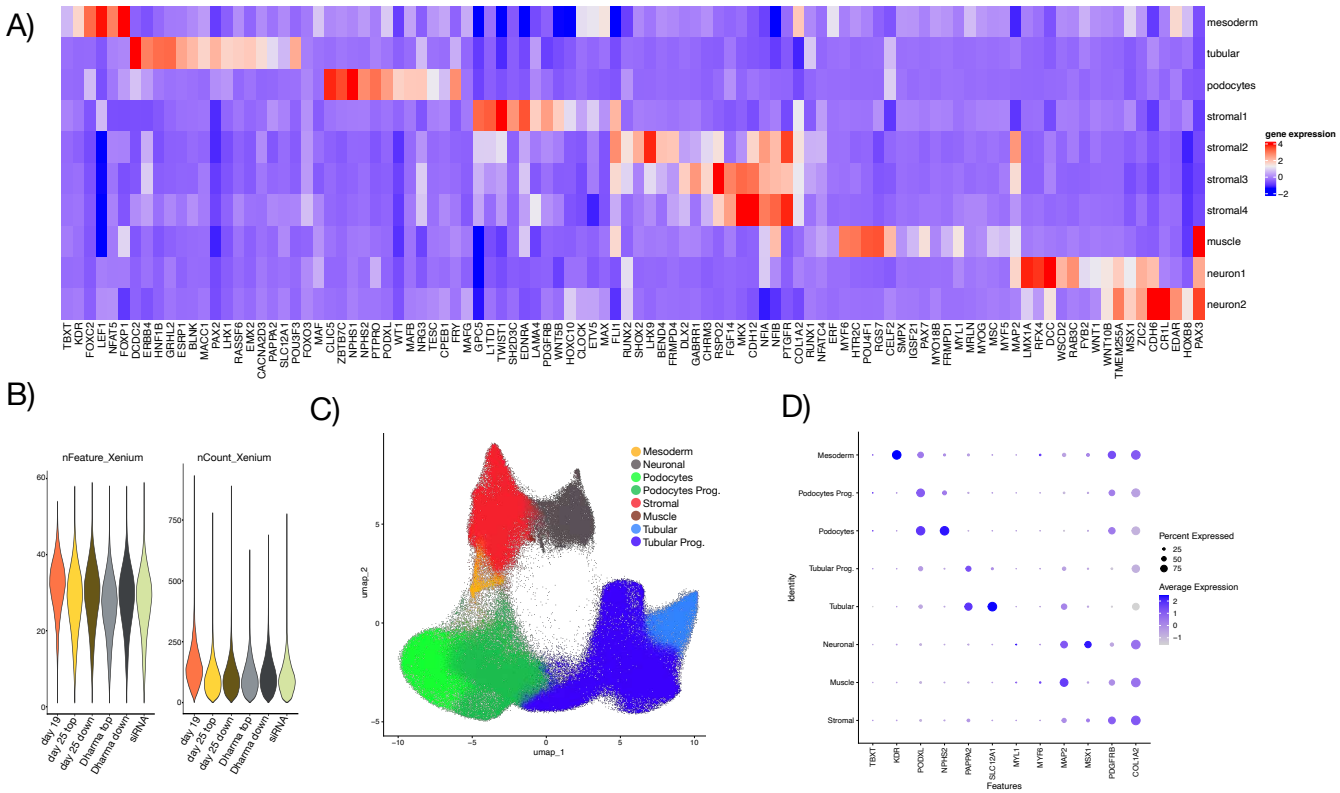

Figure S9. Xenium spatial profiling. A) Gene expression in multiome kidney organoid data, highlighting the 100 genes and transcription factors selected for the Xenium experiment. **B)** QC for the day 19, day 25, scrambled siRNA and siRNA treated spatial data. **C)** UMAP shows the cell types of the xenium data. **D)** Dot plots show the markers of cell types of the xenium data.

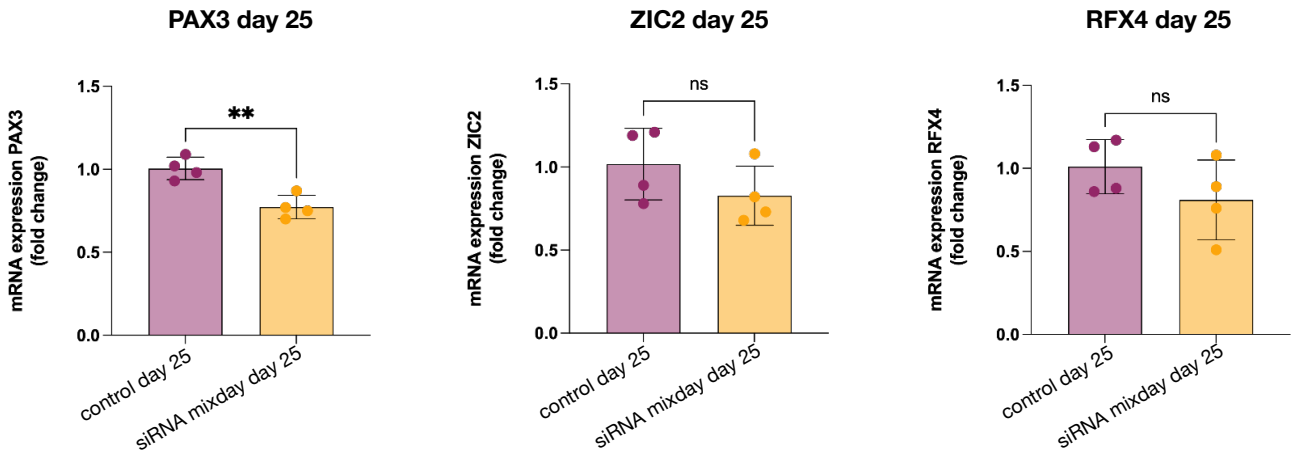

Figure S10. mRNA expression of genes targeted by siRNA experiments. Statistical test using unpaired *t*-test with bars representing mean ± sd; asterisks indicate P-values of <0.01 (**).

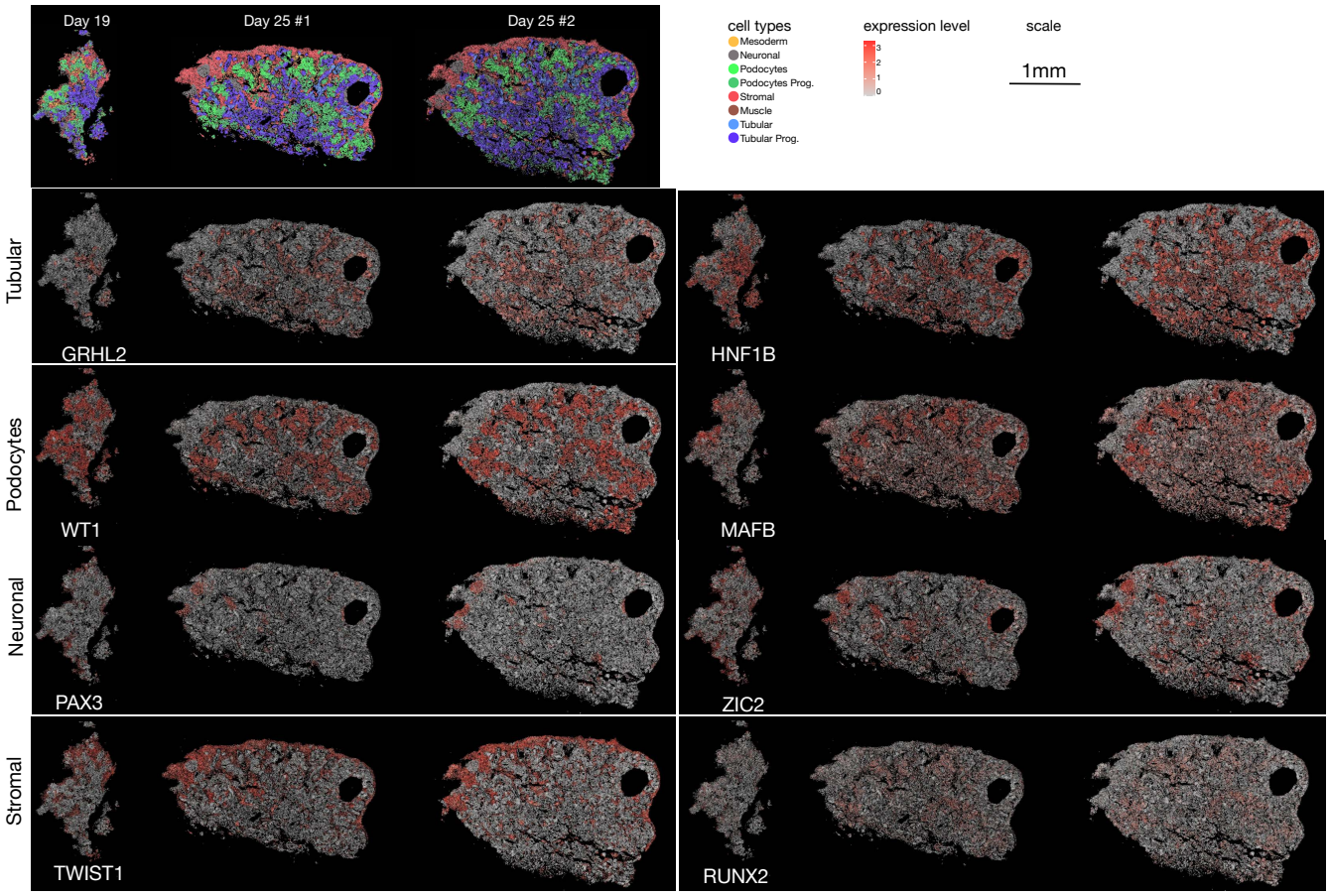

Figure S11. Spatial expression of cell type specific transcription factors for day 19 and day 25 kidney organoids.

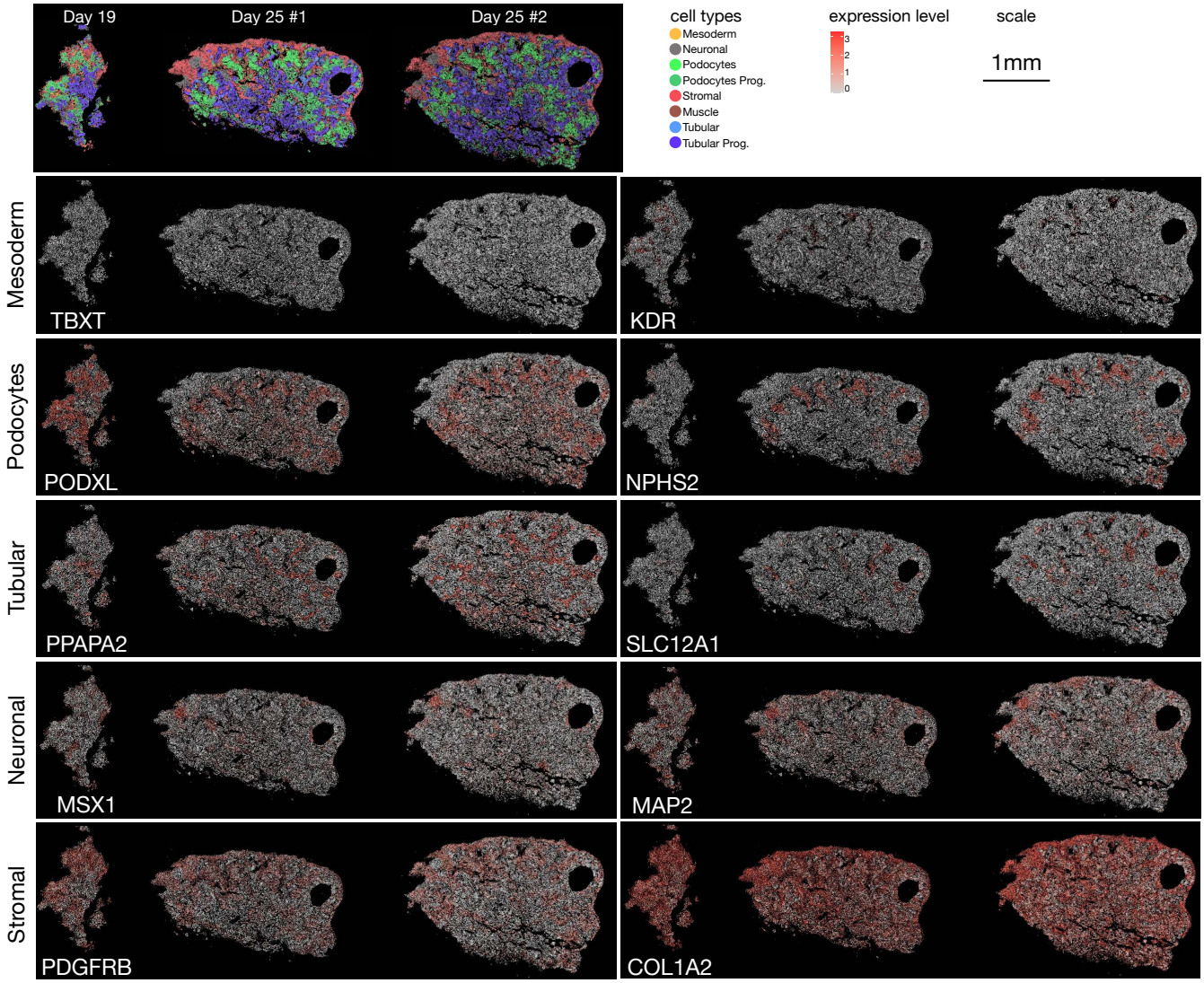

Figure S12. Spatial gene expression for cell type specific markers for day 19 and day 25 kidney organoids.

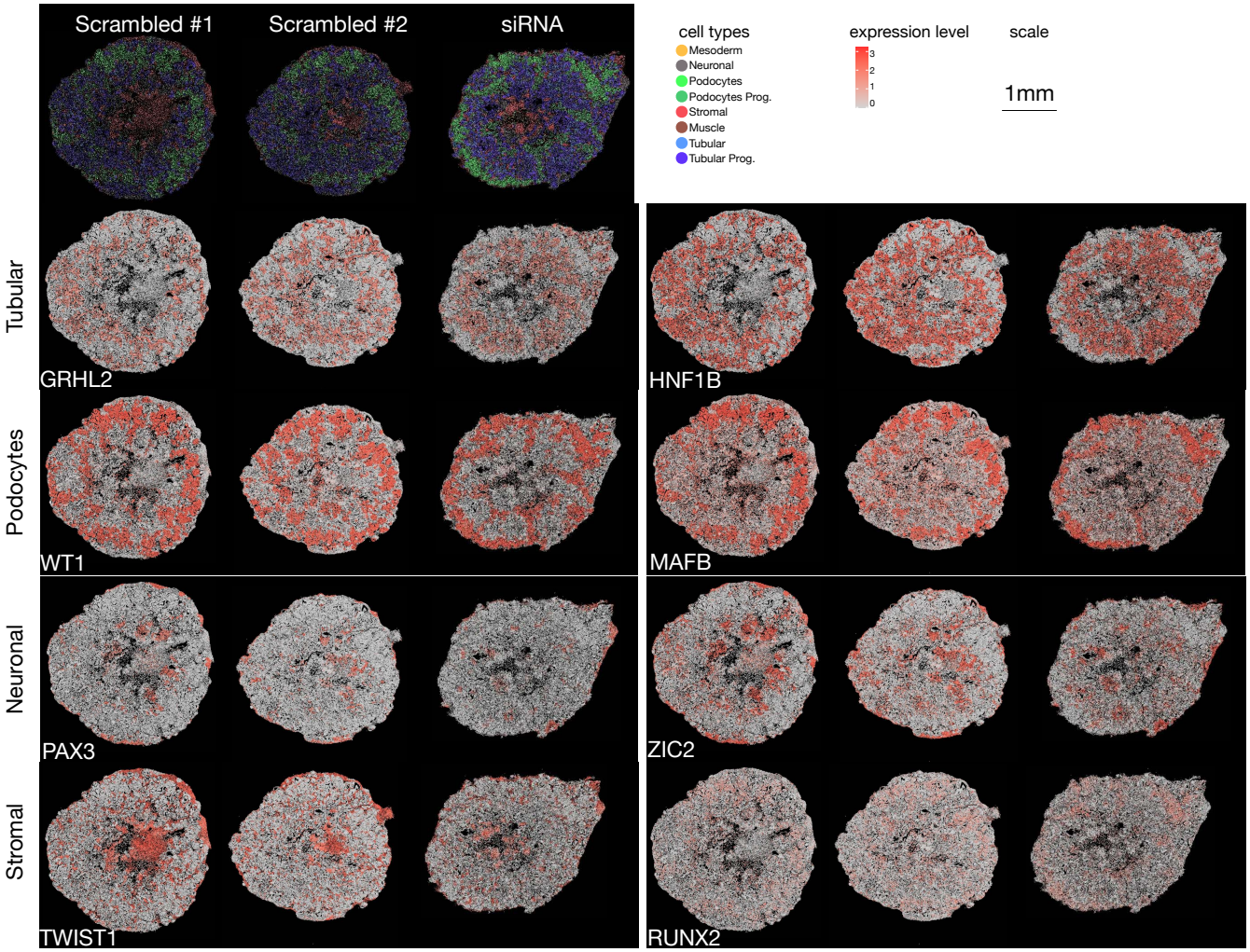

Figure S13. Spatial gene expression for cell type specific transcription factors for scrambled siRNA and siRNA treated.

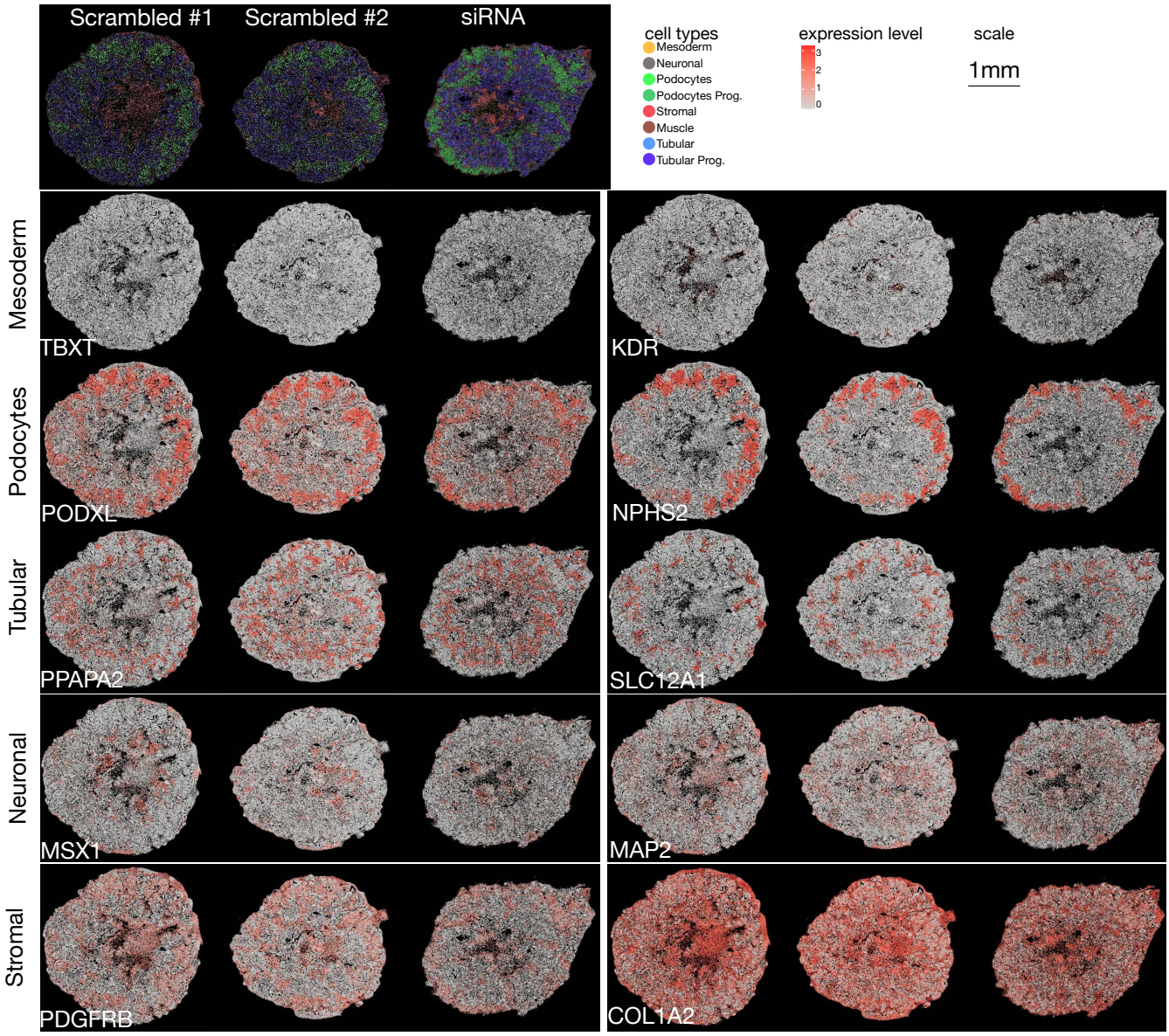

Figure S14. Spatial gene expression for cell type specific markers for scrambled siRNA and siRNA treated.

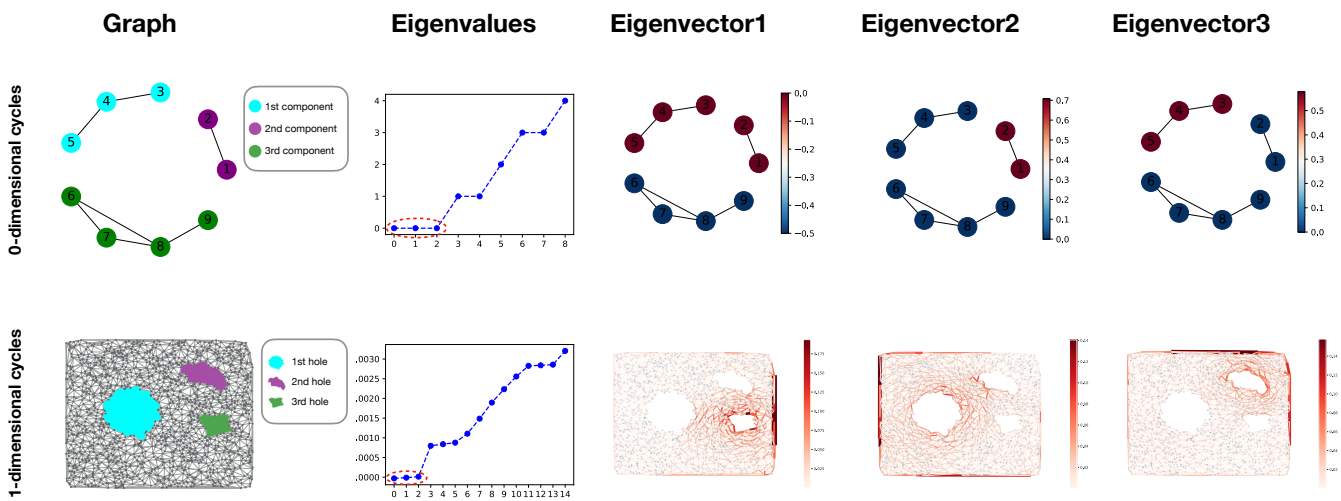

Figure S15. 0-dimensional and 1-dimensional cycles. We demonstrate the detection of 0-dimensional cycles (connected components) and 1-dimensional cycles (holes) using the 0-dimensional Hodge Laplacian and the 1-dimensional Hodge Laplacian decomposition. In the first column, the upper side displays a graph with three 0-dimensional cycles (connected components), while the bottom side shows a graph with three 1-dimensional cycles (holes). In the second column, we observe the Hodge decomposition on both the 1-simplicial complex and the 2-simplicial complex, each deriving three eigenvalues close to zero. The third, fourth and fifth columns demonstrate the zero eigenvalues corresponding to the eigenvectors around the cycles. Each of the top three 0-dimensional eigenvectors differentiates a unique 0-dimensional cycle, whereas each of the top three 1-dimensional eigenvectors is around the three 1-dimensional cycles.

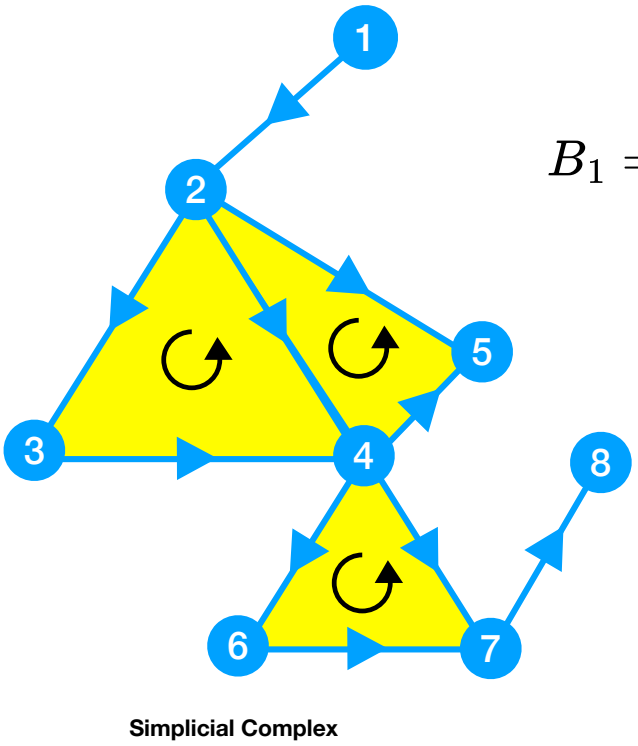

$B_1 =$

	$[1,2]$	$[2,3]$	$[2,4]$	$[2,5]$	$[3,4]$	$[4,5]$	$[4,6]$	$[4,7]$	$[6,7]$	$[7,8]$
1	-1	0	0	0	0	0	0	0	0	0
2	1	-1	-1	-1	0	0	0	0	0	0
3	0	1	0	0	-1	0	0	0	0	0
4	0	0	1	0	1	-1	-1	-1	0	0
5	0	0	0	1	0	1	0	0	0	0
6	0	0	0	0	0	0	1	0	-1	0
7	0	0	0	0	0	0	0	1	1	-1
8	0	0	0	0	0	0	0	0	0	1

$B_2 =$

	$[2,3,4]$	$[2,4,5]$	$[4,6,7]$
$[1,2]$	0	0	0
$[2,3]$	1	0	0
$[2,4]$	-1	1	0
$[2,5]$	0	-1	0
$[3,4]$	1	0	0
$[4,5]$	0	1	0
$[4,6]$	0	0	1
$[4,7]$	0	0	-1
$[6,7]$	0	0	1
$[7,8]$	0	0	0

Figure S16. Example of an ordered simplicial complex and boundary maps B_1 and B_2 representing this complex.

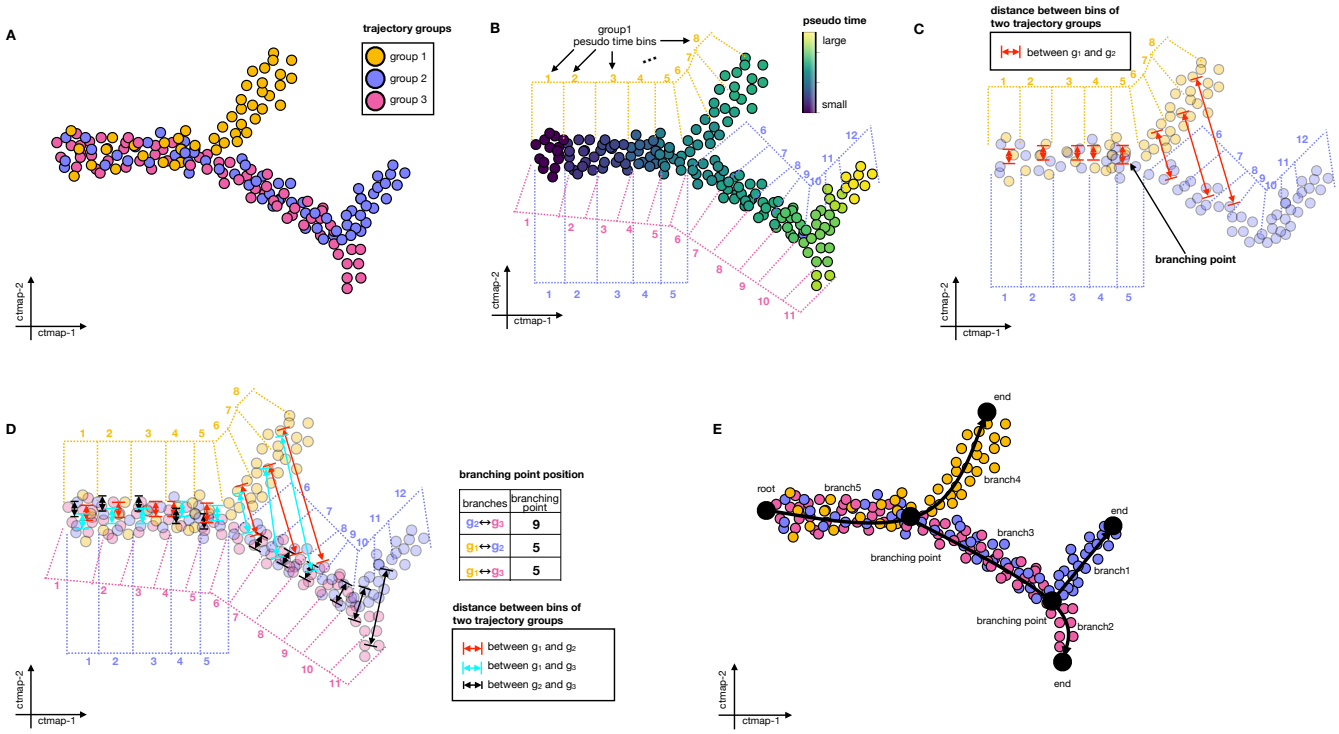

Figure S17. Schematic showing how to create a tree using edges lay in cumulative trajectory space. A) Example of three trajectory groups g_1, g_2, g_3 each with a distinct color in the cumulative trajectory space. Every dot in this embedding represents an edge in the graph (or a cell differentiation event). **B)** PHLOWER takes the mean on the pseudo-time of the vertices (cells) connected by an edge and uses this as the edge pseudo-time estimate. PHLOWER next bins the edges by considering their pseudo-times. **C)** It then estimates average edge locations for every bin, which serves as a backbone for the trajectories. It also estimates the distance between edges in two groups but with the same bin index. **D)** Distance between bins are estimated for all groups and branchings points are detected whenever the distance between edges in two groups surpasses the distances of edges within a group for a given bin In the example, bin 9 is a branching point between groups 2 and 3 and bin 5 is a branching point between groups 1 and 2 and 1 and 3. **E)** To build the final tree, PHLOWER considers the branching points with the highest values towards the lowest values to build trees in a bottom-up approach, i.e. it merges trajectory 2 and 3 at bin 9. The next branching point is 5, which connects trajectory 1 with the tree formed by 2 and 3.

names	celltype	Source
ESRP1	Tubular	Computational Gene Markers
BLNK	Tubular	Computational Gene Markers
DCDC2	Tubular	Computational Gene Markers
MACC1	Tubular	Computational Gene Markers
PAX2	Tubular	Computational Gene Markers
LHX1	Tubular	Computational Gene Markers
RASSF6	Tubular	Computational Gene Markers
EMX2	Tubular	Computational Gene Markers
CACNA2D3	Tubular	Computational Gene Markers
GRHL2	Tubular	Computational Gene Markers
ERBB4	Tubular	Computational Gene Markers
POU3F3	Tubular	Computational Gene Markers
NPHS2	Podocytes	Computational Gene Markers
CLIC5	Podocytes	Computational Gene Markers
ZBTB7C	Podocytes	Computational Gene Markers
WT1	Podocytes	Computational Gene Markers
NPHS1	Podocytes	Computational Gene Markers
PODXL	Podocytes	Computational Gene Markers
NRG3	Podocytes	Computational Gene Markers
PTPRO	Podocytes	Computational Gene Markers
MAFB	Podocytes	Computational Gene Markers
TESC	Podocytes	Computational Gene Markers
CPEB1	Podocytes	Computational Gene Markers
FRY	Podocytes	Computational Gene Markers
GPC5	Stromal1	Computational Gene Markers
L1TD1	Stromal1	Computational Gene Markers
TWIST1	Stromal1	Computational Gene Markers
SH2D3C	Stromal1	Computational Gene Markers
EDNRA	Stromal1	Computational Gene Markers
LAMA4	Stromal1	Computational Gene Markers
WNT5B	Stromal1	Computational Gene Markers
SHOX2	Stromal234	Computational Gene Markers
RSPO2	Stromal234	Computational Gene Markers
BEND4	Stromal234	Computational Gene Markers
MKX	Stromal234	Computational Gene Markers
LHX9	Stromal234	Computational Gene Markers
PTGFR	Stromal234	Computational Gene Markers
DLX2	Stromal234	Computational Gene Markers
GABRR1	Stromal234	Computational Gene Markers
FGF14	Stromal234	Computational Gene Markers
CDH12	Stromal234	Computational Gene Markers
CHRM3	Stromal234	Computational Gene Markers
FRMPD4	Stromal234	Computational Gene Markers
LMX1A	Neuron12	Computational Gene Markers
WSCD2	Neuron12	Computational Gene Markers
RFX4	Neuron12	Computational Gene Markers
WNT10B	Neuron12	Computational Gene Markers
RAB3C	Neuron12	Computational Gene Markers
FYB2	Neuron12	Computational Gene Markers
TMEM255A	Neuron12	Computational Gene Markers

names	celltype	Source
CR1L	Neuron12	Computational Gene Markers
EDAR	Neuron12	Computational Gene Markers
DCC	Neuron12	Computational Gene Markers
WNT1	Neuron12	Computational Gene Markers
CDH6	Neuron12	Computational Gene Markers
SMPX	Muscle	Computational Gene Markers
IGSF21	Muscle	Computational Gene Markers
HTR2C	Muscle	Computational Gene Markers
PAX7	Muscle	Computational Gene Markers
MYO18B	Muscle	Computational Gene Markers
FRMPD1	Muscle	Computational Gene Markers
MYF6	Muscle	Computational Gene Markers
MYL1	Muscle	Computational Gene Markers
CELF2	Muscle	Computational Gene Markers
MRLN	Muscle	Computational Gene Markers
POU4F1	Muscle	Computational Gene Markers
RGS7	Muscle	Computational Gene Markers
FOXC2	Tubular	Transcription factors
FOXP1	Tubular	Transcription factors
FOXO3	Tubular	Transcription factors
MAF	Tubular	Transcription factors
HNF1B	Tubular	Transcription factors
MAFG	Podocytes	Transcription factors
ERF	Stromal1	Transcription factors
CLOCK	Stromal1	Transcription factors
ETV5	Stromal1	Transcription factors
MAX	Stromal1	Transcription factors
FLI1	Stromal1	Transcription factors
NFIA	Stromal234	Transcription factors
NFAT5	Stromal234	Transcription factors
RUNX1	Stromal234	Transcription factors
NFATC4	Stromal234	Transcription factors
NFIB	Stromal234	Transcription factors
RUNX2	Stromal234	Transcription factors
PAX3	Neuron12	Transcription factors
HOXB8	Neuron12	Transcription factors
LEF1	Neuron12	Transcription factors
ZIC2	Neuron12	Transcription factors
HOXC10	Neuron12	Transcription factors
MYOG	Muscle	Transcription factors
MSC	Muscle	Transcription factors
MYF5	Muscle	Transcription factors
TBXT	Mesorderm	Literatuer Cell Markers
KDR	Mesorderm	Literatuer Cell Markers
PAPPA2	Tubular	Literatuer Cell Markers
SLC12A1	Tubular	Literatuer Cell Markers
MSX1	Neuron	Literatuer Cell Markers
MAP2	Neuron	Literatuer Cell Markers
PDGFRB	Stromal	Literatuer Cell Markers
COL1A2	Stromal	Literatuer Cell Markers

Table S1. List of genes used in the Xenium spatial profiling panel. Source indicates if marker were based on computational markers from the mulitome data; literature markers or TFs predicted by PHLOWER and scMEGA.